263 (2026) 214490

Contents lists available at ScienceDirect

Geoenergy Science and Engineering

journal homepage: www.sciencedirect.com/journal/geoenergy-science-and-engineering

Scenario-based data assimilation framework to improve production estimates for geologically complex geothermal reservoirs

Guofeng Song [a], Sebastian Geiger [a,*], Denis Voskov [a,b], Hemmo A. Abels [a], Philip J. Vardon [a]

[a] Department of Geoscience & Engineering, Delft University of Technology, Stevinweg 1, Delft, 2628 CN, the Netherlands
[b] Department of Energy Science & Engineering, Stanford University, Stanford, CA, 94305, USA

ARTICLE INFO

Keywords:
Geological scenarios
Channelized fluvial geothermal system
Rapid reservoir modeling
Ensemble smoother with multiple data assimilation
Uncertainty quantification
Geothermal energy production

ABSTRACT

Geothermal energy has the potential to decarbonize heating, cooling, and power production. However, managing the efficient and sustainable exploitation of geothermal resources is challenging due to the limited data availability, which restricts our ability to characterize and quantify the multi-scale, hierarchical geological structures of the hosting reservoirs. In this study, we propose a scenario-based data assimilation framework that enables the efficient modelling of multiple complex geological scenarios and is linked to flow and heat transfer simulations for subsequent uncertainty analysis. This framework is based on an ensemble smoother with multiple data assimilation (ESMDA) and demonstrated on a channelized fluvial geothermal reservoir. By improving the open-source Rapid Reservoir Modelling (RRM) tool, we efficiently create multiple deterministic fluvial geothermal reservoir scenarios that honors facies along well paths in a probabilistic manner by randomly selecting, cropping, and stacking channelized layers from the layer template library. Petrophysical properties for each scenario are then modelled using geostatistics to generate a geologically plausible and sufficiently diverse ensemble of reservoir realizations. The multiple scenarios and corresponding ensemble realizations are then subjected to heat and fluid flow simulations using the open-source Delft Advanced Research Terra Simulator (open-DARTS) to quantify the uncertainty of production temperatures and reservoir pressures. Finally, ESMDA is employed to assimilate temperature and pressure profiles at the injection well, monitoring borehole, and production well across all members of the ensemble realizations for the different geological scenarios. We demonstrate the applicability of our framework using a synthetic, yet geologically consistent, case study of a low-enthalpy geothermal system where heat is produced from a geothermal doublet located in a channelized fluvial sandstone reservoir. The framework enables the falsification of geological scenarios with poor data assimilation performance that is unlikely to reflect the actual reservoir architecture, and supports the identification of plausible geological scenarios that are more likely to represent the subsurface geology based on the deviation of modelled and observed well temperature and pressure profiles. The workflow offers an efficient way to constrain geological uncertainties inherent to geologically complex geothermal reservoirs and improve the forecasting of production temperatures and pressure differences.

1. Introduction

Geothermal energy can play an important role in the energy transition by decarbonizing heating and cooling, which account for nearly 50% of the total energy consumption in the global north (Moya et al., 2018). In particular, direct-use low-enthalpy geothermal systems for space heating are gaining significant attention in Europe (Anderson and Rezaie, 2019; Limberger et al., 2018; Lund and Toth, 2021). These systems are often exploited using multi-well configurations, such as doublets, with one well for cold water injection and the other for hot water production (Babaei and Nick, 2019; Daniilidis et al., 2021; Wang et al., 2021). Similar to other subsurface resources, long-term geothermal exploitation is subject to considerable uncertainty due to the multi-scale and hierarchical geological heterogeneities inherent to subsurface reservoirs, insufficient knowledge about the spatial distribution of these heterogeneities, and inadequate conceptual and

* Corresponding author.
E-mail address: S.Geiger@tudelft.nl (S. Geiger).

https://doi.org/10.1016/j.geoen.2026.214490
Received 9 November 2025; Received in revised form 20 February 2026; Accepted 8 April 2026
Available online 12 April 2026

mathematical models of the fluid-rock interactions that control flow behaviors (Witter et al., 2019). To explore and constrain these uncertainties and their impact on production rates and temperatures, reservoir models are created based on data interpretation and empirical correlations. These models aim to account for the limited data availability and our incomplete understanding of the subsurface geology (Ringrose and Bentley, 2016). By numerically simulating heat and fluid flow for these reservoir models, the different production behaviors can be explored, and uncertainties that impact technical risks such as early thermal breakthrough, short operational lifespan, or high maintenance costs can be assessed and quantified. To mitigate these risks, support the decision-making during operations, and optimize the overall performance of a geothermal system, it is essential to effectively capture, quantify, and constrain uncertainties (Daniilidis et al., 2021; Hoteit et al., 2023; Juliusson and Bjornsson, 2021).

One of the major technical factors contributing to uncertainty in the production forecasts is geological uncertainty, which needs to be adequately represented in the reservoir modeling (Mendez et al., 2024; Yousefzadeh et al., 2020). There are three distinct approaches for uncertainty handling during reservoir modeling (Bentley and Smith, 2008). Rationalist approach: the method selects a preferred reservoir model as base case and then adds a range of uncertainty around the base case to generate the 'upside' and 'downside' cases. The base case is a reference model against which alternative models are compared. Multiple stochastic approach: equiprobable realizations are generated probabilistically using geostatistical simulation. A realization is a single instance generated within a specific reservoir scenario. Each realization is populated with the continuous property fields that exhibit spatial variability (e.g., porosity, permeability and thermal properties). Multiple realizations are produced for the same scenario to reflect the uncertainty in the continuous properties while keeping the overall reservoir architecture fixed. Multiple-deterministic scenario modeling approach: Geological scenarios are designed as deterministic representations of various discrete subsurface concepts, rather than relying on statistical sampling based on a single initial scenario. Each scenario provides an alternative depiction of the reservoir architecture, effectively capturing large-scale geological uncertainty. For example, in a fluvial reservoir, variations in channel belt size, channel sinuosity, number, connectivity, and stacking lead to a diverse range of geological scenarios (Song et al., 2024). Scenario modeling can also be combined with the multiple stochastic approach, where deterministic scenarios are first designed and then multiple probabilistic realizations are generated within each scenario through geostatistical method to populate heterogeneous porosity and permeability into different domains (Bentley and Smith, 2008).

With regard to scenario uncertainty analysis for production forecasts in geothermal systems, previous studies mostly focused on ensemble realizations around a single geological scenario to evaluate the range of possible production curves. For example, Wang et al. (2023) employed the open-source Delft Advanced Research Terra Simulator (open--DARTS) to perform an uncertainty quantification, considering variability in porosity-permeability distributions, salinity, and rock conductivities and their impact on produced energy and net present value of a low-enthalpy channelized fluvial geothermal system. Babaei and Nick (2019) conducted 2600 numerical simulations of a low-enthalpy geothermal system considering different variances and correlation lengths in the statistical models that describe the porosity distribution. However, these studies only considered a single geological scenario, which, as discussed above, usually cannot adequately capture inherent geological uncertainty. Reservoir architecture, i.e., the multi-scale geometry of different geological structures and their spatial interaction, plays a crucial role in the development of subsurface energy systems, not only in oil and gas exploration but also in geothermal production (Bond, 2015). Schulte et al. (2020) conducted a multiple-objective optimization for a geothermal doublet considering various geological scenarios, for example, in the fault models for the reservoir. Significant variations in bottom hole pressure differential (>3000 kPa) were observed across the different geological scenarios. The optimization of well positions and re-injection temperatures was highly sensitive to underlying scenarios. Wang et al. (2021) showed that the presence of shale facies and overburden layers can extend the lifetime of low-enthalpy geothermal systems. Aghaei et al. (2024) employed meander-belt stratigraphic architectures to investigate the impact of sedimentary heterogeneity on the efficiency of geothermal doublets. Their findings revealed that geological heterogeneities shaped by river hydrodynamics, channel abandonment, and meander transformation significantly impact the shape of the thermal plume and cold-water breakthrough. Therefore, the inherent uncertainty in reservoir architecture should be explored, and its impacts on geothermal production quantified. Addressing this uncertainty in reservoir scenarios requires rapid and flexible tools for geological scenario construction.

Rapid Reservoir Modeling (RRM) provides a rapid way for such scenario modeling. RRM is an open-source, sketch-based modeling tool with an intuitive interface, enabling users to explore and rapidly create geologically consistent 3D reservoir model scenarios from 2D sketches (Jacquemyn et al., 2021; Petrovskyy et al., 2023). RRM can explore deterministic scenarios quickly, especially for data-poor environments like geothermal systems (Baird et al., 2023). Scenario-based modelling using RRM can be combined with the stochastic modeling method to populate heterogeneous properties within different domains for each reservoir scenario, so that uncertainties from both reservoir architecture and petrophysical data are captured (Song et al., 2024).

To quantify and constrain uncertainty in the production forecasts caused by the geological uncertainty inherent to a geothermal reservoir, inversion approaches offer a promising strategy for adjusting geological models with real-world observations, such as well temperatures, pressure, electromagnetic data and seismic data (Athens and Caers, 2019; Hermans et al., 2018; Oudshoorn et al., 2024). This process, also known as data assimilation, usually combines prior equiprobable realizations for a given scenario, forward simulations, and field observations to generate revised posterior realizations for uncertainty estimation (Seabra et al., 2024). Commonly used data assimilation methods include gradient-based approaches, Markov Chain Monte Carlo (MCMC), and ensemble-based methods (Evensen et al., 2022). Tian et al. (2024) utilized the adjoint method to efficiently compute the gradient required in the Randomized Maximum Likelihood (RML) framework applied to history matching in geothermal reservoirs. While the adjoint method improves computational efficiency, it is not available as standard in many reservoir simulators. If adjoint methods are not available, gradient approximations are needed; they are, however, computationally expensive for high-dimensional parameter inversion, particularly when optimization must be performed independently for each realization to construct a posterior ensemble. Iterative Ensemble Kalman Filter (EnKF) approaches (Liu et al., 2020) avoid the need for costly gradient computations but rely on repeated linearization, which can cause ensemble collapse in strongly nonlinear problems such as geothermal systems with temperature-dependent fluid properties, coupled flow and heat transport processes, and complex reservoir architectures. Ensemble Smoother with Multiple Data Assimilation (ESMDA) (Emerick and Reynolds, 2013) is computationally efficient, flexible and capable of integrating multisource data. ESMDA has gained increasing popularity in subsurface characterization of properties, and is particularly effective for weakly nonlinear and high-dimensional problems as they avoid explicit computation of the Jacobian matrix while maintaining ensemble diversity. ESMDA applies parameter updates gradually over multiple assimilation steps by inflating observation error covariance. This tempered update strategy improves numerical stability, preserves ensemble variability, and provides more robust performance in nonlinear systems. It has been demonstrated that ESMDA generates an ensemble of plausible posterior realizations for a given scenario where each realization aligns reasonably well with observed data (Chen et al., 2024; Oudshoorn et al., 2024; Saifullin et al., 2024; Wu et al., 2021).

However, the variability among ensemble realizations only captures uncertainties stemming from petrophysical property. If the realizations are based on a geological scenario that poorly represents the actual reservoir architecture, then the forecasts become unreliable. Thus, data assimilation should consider geological uncertainties in reservoir architectures such as channel belt size, channel sinuosity, connectivity, stacking, etc., i.e., consider different geological scenarios and not only variability in property distributions.

To date, only a small number of data assimilation studies address uncertainty updates while also considering multiple geological scenarios, especially for the geologically complex 3D reservoir systems like fluvial reservoirs. Athens and Caers (2019) created prior geological realizations of a basin-scale geothermal system where architectural elements like basin depth, fault dip, and basin asymmetry are simply characterized by uniform statistics. They employed Bayesian Evidential Learning (BEL) to reduce the uncertainty in the temperature gradient, using the temperature distribution of a single well temperature as a constraint. Cao et al. (2018) and Guo et al. (2021) used multiple-point geostatistics (MPS) to model 2D channelized structures conditioned on direct measurements. By integrating iterative ensemble smoothers or ESMDA with MPS via pilot points, they improved flow and transport modeling by honoring observations and conceptual geological models (e.g., channel frameworks) after assimilation. Although MPS can generate complex reservoir models, relying on a single training image restricts the variability of reservoir architectures. Ling and Jafarpour (2024), and Jiang and Jafarpour (2020), utilized deep learning techniques such as Variational Autoencoders (VAEs) and Generative Adversarial Networks (GANs) to convert the complex, non-Gaussian subsurface properties into a low-dimensional Gaussian latent space across multiple geological scenarios. ESMDA was then used to calibrate the latent parameters with production data, and the updated latent space was used to reconstruct subsurface properties that remain consistent with the predefined geological continuity models. The results demonstrate the potential of VAE and GAN for improving the representation and reconstruction of complex spatial patterns in subsurface flow model calibration. However, these deep learning techniques still require validation on 3D geologically complex reservoir models that incorporate a wide range of plausible geological scenarios to ensure effective parameterization. In summary, the combination of scenario construction and data assimilation is essential to explore and potentially falsify geological scenarios, rather than merely adjusting petrophysical properties.

This study focuses on geologically complex fluvial geothermal reservoirs, inspired by the Delft campus geothermal project (Geothermie Delft). It was established to provide thermal energy for the campus and parts of the city of Delft (Vardon et al., 2024; Voskov et al., 2024). The project consists of a doublet system targeting the fluvial Lower Cretaceous Delft sandstone formation at a depth of slightly over 2 km beneath the campus (Willems et al., 2020). The Delft Sandstone reservoir is interpreted as stacked distributary-channel deposits in a lower coastal plain environment, resulting in extensive sandstone sequences (Vardon et al., 2024; Wang et al., 2023; Willems et al., 2020). The key research question is how to best capture geological uncertainty in geologically complex geothermal reservoirs and how to quantify and constrain uncertainty in geothermal production to enable reliable forecasts. We propose a scenario-based data assimilation framework that integrates efficient geological modeling, high-fidelity production simulation, and ensemble-based data assimilation to explore, quantify, and constrain uncertainties in fluvial geothermal systems. Unlike traditional methods that rely on a single reservoir scenario, this framework leverages multiple scenarios to quantify and constrain production uncertainty by simultaneously addressing uncertainties in reservoir architectures and properties. An efficient geological modeling approach that combines scenario-based Rapid Reservoir Modeling (RRM) with stochastic modeling to effectively capture geological uncertainties in reservoir architecture and petrophysical properties. An ensemble of deterministic fluvial geothermal reservoir scenarios that honors the available well data such as facies distributions along well-path is efficiently generated in a probabilistic manner by randomly selecting, cropping, and stacking channelized layers from the layer template library. An ensemble of realizations with uncertain petrophysical properties is generated through Sequential Gaussian Simulation (SGS) for each reservoir scenario. One realization of the reference reservoir scenario with specific channel features is selected as the synthetic 'truth' case and its simulated production data were taken as the 'observed' data against which all other simulations are compared. Open-source DARTS is employed on multiple reservoir scenarios and corresponding ensemble realizations to conduct flow and heat transfer simulations, and temperature and pressure responses are obtained. Finally, ESMDA is utilized to assimilate 'observed' data and update the ensemble of realizations for each scenario. Through scenario-based data assimilation, reservoir scenarios with the lower ESMDA errors are identified as the plausible scenarios that provide more reliable production estimates. Scenarios with poor data assimilation performance are effectively falsified, indicating that they are unlikely to represent the true reservoir architecture. Production estimates become more reliable when based on a range of plausible reservoir scenarios, rather than being constrained to a single base case, which may introduce bias.

The remainder of this paper is organized as follows: Section 2 details the methods of geological modeling and data assimilation. Section 3.1 demonstrates the construction of the reference case, along with the ensemble of prior scenarios and their corresponding realizations. Section 3.2 quantifies production uncertainty by analyzing the influence of reservoir architectures and the variability of heterogeneous porosity and permeability within the channels for each scenario. Section 3.3 applies the proposed scenario-based data assimilation framework across multiple scenarios, identifying plausible scenarios based on root mean square errors (*RMSE*) that are more likely to yield reliable production estimates and falsifying scenarios with poor data assimilation performance. Sections 4 and 5 present the discussions and conclusions, respectively.

2. Methodology

The scenario-based data assimilation framework involves two key aspects: First, efficiently generating model ensembles representing fluvial reservoirs with varying channel geometries and heterogeneous properties, and, second, conducting data assimilation across different geological scenarios and stochastic realizations associated with each scenario.

2.1. Geological modeling

We combined scenario-based RRM modeling with stochastic modeling to efficiently construct geologically diverse reservoir scenarios, along with their corresponding equiprobable realizations for each scenario. The geological modelling is inspired by the Delft Sandstone reservoir, but could be regarded analogue of any channelized reservoir. Our synthetic reservoir models have a dimension of 3 km $\times$ 2 km $\times$ 120 m.

2.1.1. Scenario-based geological modeling

RRM is an open-source, sketch-based modeling tool that allows users to intuitively create geologically consistent 3D reservoir models from 2D sketches using a sketch-based interface and modeling (SBIM) (Jacquemyn et al., 2021). The concept of surface-based reservoir modeling is utilized (Jacquemyn et al., 2019), meaning that all geological heterogeneities are represented by surfaces that define geological domains, i.e., enclosed volumes representing a geological structure. These surfaces are hierarchical and multi-scale, representing, for example, faults, stratigraphic surfaces, facies, laminae, or diagenetic bodies. Geological operators in RRM ensure that the surfaces interact in

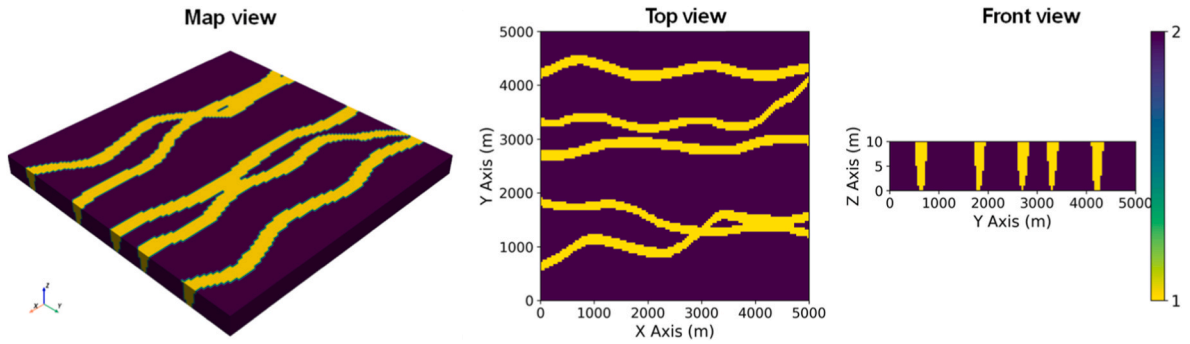

Fig. 1. 3D, map, and cross-sectional views of a template for channelized fluvial sedimentary layer generated in RRM (1 = sand, 2 = mudstone).

Table 1
Fluvial layer template parameters.

Items	Values
Layer template size	5000 m × 5000 m × 10 m
Facies	sand, mudstone
Channel sinuosity	low, mid, and high
Channel belt width	200 m, 500 m, and 800 m
Channel belt height	10 m
Layer NTG	0, 20%, 40%, 60%, and 80%

a geologically consistent way. RRM is specifically designed to very quickly create, test, and compare different geological concepts rather than spending significant efforts to build detailed reservoir models using geostatistical methods. RRM is therefore well-suited for situations where data availability is limited, such as geothermal systems, because it allows users to quickly explore a broad range of different geological scenarios that honor the data. The resulting models can be exported using standard grid formats for further processing, including numerical simulations using commercial and research software.

RRM is employed to create 180 templates for geological layers with varying channel sinuosity, channel belt width and Net-to-Gross (NTG, i.e. sand ratio). Fig. 1 shows 3D, top, and front views of an example template for a geological layer containing fluvial channels that was created in RRM. The yellow regions indicate the channels containing sand facies, and the purple regions represent the mudstone facies. The size for this particular template is 5 km × 5 km × 10 m, and its areal extent is larger than that of the target reservoir in the Delft Sandstone. Using a uniform experimental design, we created a total of 180 templates considering features such as channel belt width, layer NTG, and channel sinuosity (Table 1). The channel sinuosity has three levels: low, mid, and high, while the channel belt width is categorized into three

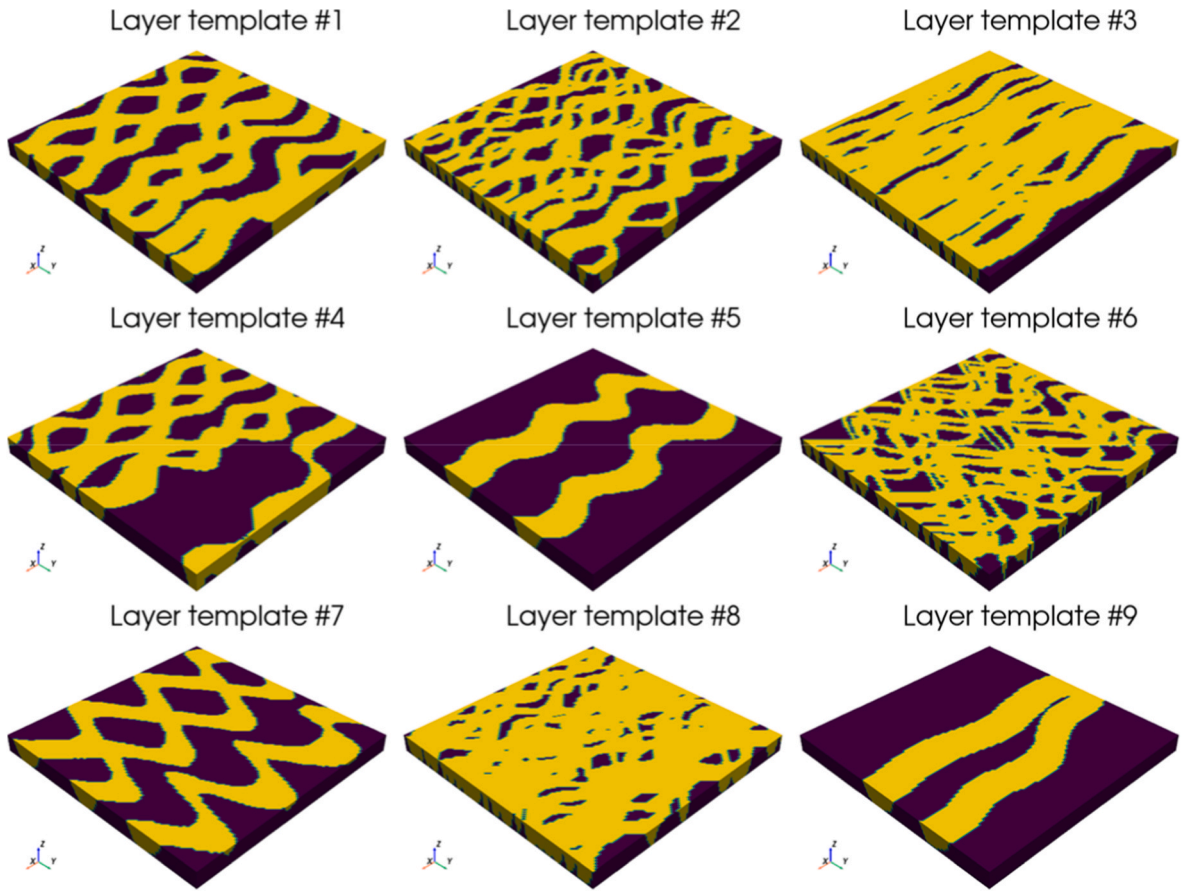

Fig. 2. Nine illustrative templates of channelized fluvial layers drawn in RRM to be stacked to form the channelized fluvial reservoir scenarios.

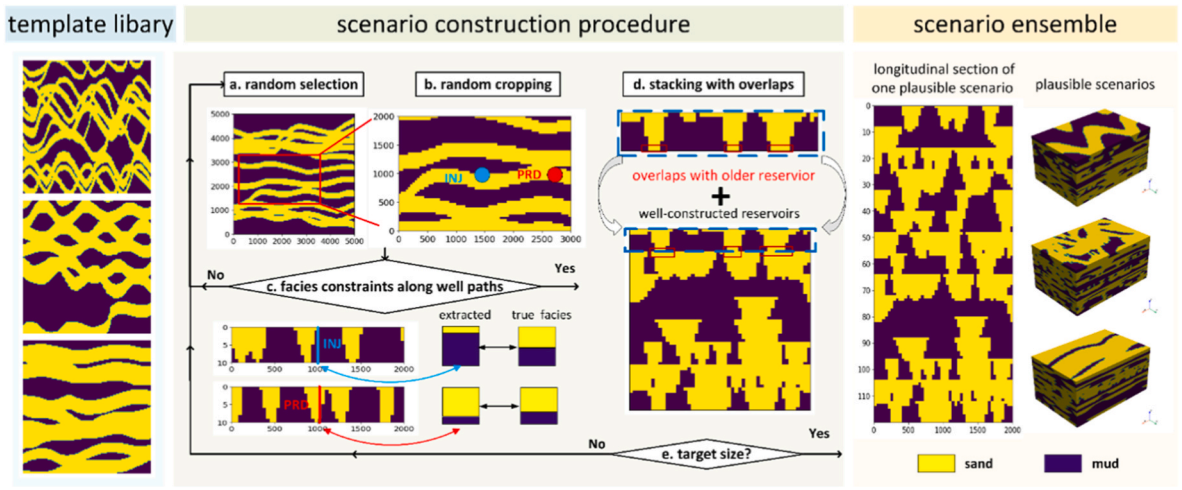

Fig. 3. Procedure for constructing multiple geological scenarios constrained by well information. (a) A layer template is randomly selected from a predefined template library. (b) A sub-region is randomly cropped from the selected template. (c) The facies at well locations within the sub-region are compared against the reference well information; the sub-region is retained if consistent. (d) The accepted sub-region is stacked on top of the existing reservoir model. An overlap allows younger channels to partially erode older ones, such that sand facies in younger layers may overwrite those in underlying units. This process is repeated until the target reservoir height is reached. By using the same well facies constraints, an ensemble of geological scenarios can be generated.

levels: 200 m, 500 m, and 800 m. The layer NTG has five levels: 0%, 20%, 40%, 60%, and 80%. Consequently, the final library consists of 180 templates, representing diverse geological heterogeneities inherent in channelized fluvial geothermal reservoirs. Fig. 2 shows nine of these templates. For example, layer template #1 features a mid-sinuosity channel, a channel belt width of 500 m, and an NTG of 60%.

Fig. 3 illustrates the construction of 3D geological scenarios using the layer templates. A template is randomly selected from the library, and a sub-region is cropped from the template to match the target area size of the reservoir. In our case, the target size in the horizontal direction is 3 km × 2 km, i.e. smaller than the areal dimension of the template (5 km × 5 km). The exact location where this sub-region is cropped is random and hence introduces another level of uncertainty to the final model. The extracted sub-region is then evaluated to ensure it honors facies along the well path. As shown in Fig. 3(c), we compare the facies at injection and production well locations within the sub-region to the 'truth' facies at the same position in the reference reservoir model. If the NTG at the well positions of the sub-region matches that computed from the reference case, the sub-region is retained. This matching process implies that the facies at the injection and production wells within the sub-region are identical to the facies profiles in the 'truth' case. The accepted sub-region is regarded as one additional reservoir layer, which is stacked onto the previously assembled reservoir layers that also meet the criteria until the cumulative height of the 3D model reaches the target of 120 m. Adjacent layers are not simply stacked but overlapped to mimic the deposition of fluvial sediments, where younger channels can erode older ones. Overlapping ensures that portions of the sandstones in the upper layer replace lithologies in the lower layer, preserving vertical connectivity and the associated heterogeneity. The geological scenarios with a wider set of fluvial features–such as point bars, channel lags, levees, and crevasse splays–can be generated if the layer template library is enriched with more facies. This study assumes two lithologies as a proof-of-concept: the channel belt is characterized by sand facies, and the out-of-channel domain is characterized by mudstone facies.

The proposed geological modeling approach is both efficient and flexible. Especially, fluvial layer templates with different channel features are quickly constructed using RRM. It enables the rapid creation of ensembles of diverse deterministic geological scenarios, rather than limiting analysis to a single base case or a limited number of deterministic scenarios. Through a sequence of random selection, cropping, constraint application and stacking operations, this method ensures the generation of geologically consistent scenarios that fully honor well data in a probabilistic way. Our approach integrates deterministically selected scenarios with probabilistic modelling, which enables a more comprehensive uncertainty quantification that considers both, uncertainty in reservoir architecture and uncertainty in petrophysical data, i.e. our approach does not rely on a single base case or a couple of deterministic scenarios, or relies merely on modelling petrophysical properties using geostatistical means.

2.1.2. *Sequential Gaussian Simulation*

Once the geological scenarios are constructed, the sand facies within the channel domain and the mudstone facies in the out-of-channel domain are given for each scenario. Porosity and permeability distributions are then assigned to each facies using Sequential Gaussian Simulation (SGS), a classic stochastic modeling method for continuous variable distributions which honors both known sample values and the variogram model (Verly, 1993). We apply SGS to the permeable sand facies only and analyze the corresponding variogram function using porosity data for the Delft Sandstone from well GT-02 (Voskov et al., 2024; Willems et al., 2020). A spherical variogram model is employed to characterize the spatial variability of porosity in sand facies. The model assumes no nugget effect (nugget = 0), and the sill is set to 1, corresponding to the variance of the normalized porosity field. The model incorporates anisotropic correlation ranges, with a maximum range of 1600 m along the azimuth of 90° (east-west direction) and a minor range of 550 m. The vertical range is set to 10 m, reflecting the higher variability in the vertical direction due to depositional heterogeneity. This variogram is utilized in SGS to generate geostatistical realizations of porosity. The detailed procedure can be found in (Bai and Tahmasebi, 2022; Nowak and Verly, 2004). Using the porosity-permeability relationship derived from core analysis at well GT-02 (Voskov et al., 2024; Willems et al., 2020), permeability distributions are calculated for each realization based on the following expression

$$\log_{10}(k) = -3.523\cdot10^{-7}\cdot\phi^5 + 4.278\cdot10^{-5}\cdot\phi^4 - 1.723\cdot10^{-3}\cdot\phi^3 + 1.896\cdot10^{-2}\cdot\phi^2 + 0.333\cdot\phi - 3.222. \quad (1)$$

Each scenario contains an ensemble of equiprobable porosity realizations with corresponding permeability distributions for the sand facies, honoring both well data constraints and the reservoir architecture for the given scenario.

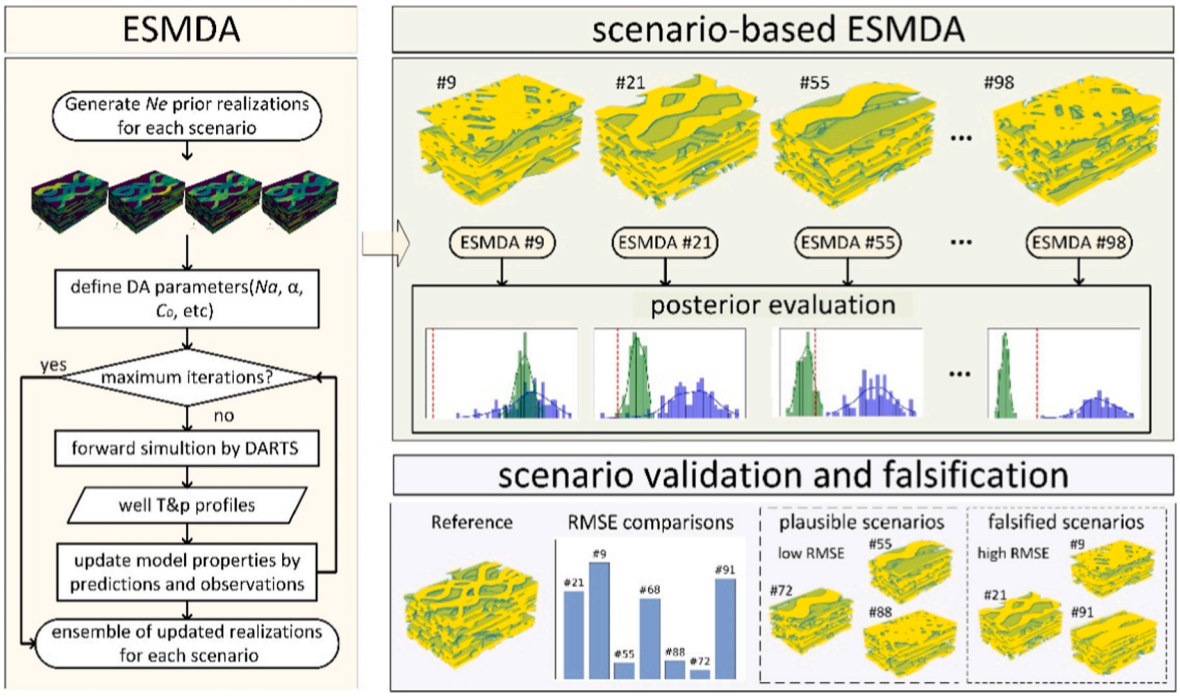

Fig. 4. Scenario-based data assimilation for geologically complex geothermal reservoirs.

2.2. Forward modeling

Reservoir simulation of low-enthalpy geothermal systems, such as the Delft Campus Geothermal Project, is based on the standard mass and energy conservation equations for slightly compressible single-phase flow (Chen et al., 2025b; Voskov et al., 2024; Wang et al., 2023). In this study, we utilize the open-source Delft Advanced Research Terra Simulator (open-DARTS) to perform the simulations. DARTS has been used successfully for ensemble-based simulation in geothermal production (Chen et al., 2025b). The simulator employs a fully implicit solution method in time and uses the finite volume method and two-point flux approximation to discretize the governing equations (Wang et al., 2020). Darcy's law is applied to model fluid flow through porous media, while the heat transfer equation describes the processes of heat convection and conduction in porous media. The conservation equations can be written as follows:

$$\frac{\partial}{\partial t}(\phi\rho) - \nabla\cdot\rho v + \rho\tilde{q} = 0, \tag{2}$$

$$\frac{\partial}{\partial t}(\phi\rho U + (1-\phi)U_r) - \nabla\cdot h\rho v + \nabla\cdot(\kappa\nabla T) + h\rho\tilde{q} = 0, \tag{3}$$

where t is the time, ϕ is the porosity of porous media, ρ is the density of fluid phase, $\tilde{q}$ is the fluid rate per unit volume, U is the phase internal energy, U_r is the internal energy of rock, h is the convection coefficient and T is the temperature. The thermal conductivity of the fluid and rock is defined as

$$\kappa = \phi\kappa_f + (1-\phi)\kappa_r, \tag{4}$$

where κ, κ_r and κ_f are the thermal conduction coefficients of the overall system, the fluid phases and the solid rock, respectively. The Darcy velocity v is given by

$$v = \frac{\mathbf{K}}{\mu}\left(\nabla p - \gamma_p \nabla D\right), \tag{5}$$

where $\boldsymbol{K}$ is the permeability of porous media, μ is the fluid viscosity, p is the pressure, γ_p is the specific weight, and D is the depth.

We use pressure and enthalpy as primary variables and consider them as state variables (Wang et al., 2020), which are evaluated using the Newton–Raphson method when solving for Equations (2) and (3)

$$\frac{\partial g(\boldsymbol{\omega}_k)}{\partial \boldsymbol{\omega}_k}(\boldsymbol{\omega}_{k+1} - \boldsymbol{\omega}_k) = -g(\boldsymbol{\omega}_k). \tag{6}$$

Here, g represents the residual form of the governing equations, ω indicates nonlinear variables represented by pressure and enthalpy in this study, and the subscript k specifies the k-th nonlinear iteration. To improve computational efficiency and flexibility of the nonlinear formulation, the operator-based linearization technique is used to compute the Jacobian and residuals (Khait and Voskov, 2017). This approach transforms the discretized mass and energy conservation equations into an operator form, separating space- and state-dependent properties. The state-dependent operators are adaptively parameterized within the space of nonlinear variables using a limited number of supporting points, significantly improving the speed and robustness of highly nonlinear reservoir simulations.

2.3. Scenario-based data assimilation

We first present a data assimilation procedure to update geostatically distributed properties for one given scenario. Then it is extended to multiple scenarios, a process we refer to as scenario-based data assimilation, to gradually falsify geological scenarios, i.e. identify those scenarios that yield flow behaviours that are consistent with dynamic data and hence are more likely than other scenarios.

Ensemble Smoother with Multiple Data Assimilation (ESMDA) is employed as the inversion methodology to adjust the continuous, Gaussian-distributed petrophysical parameters within the chanalized sand bodies. Note that the ESMDA is applied only to the geostatistically generated realizations of the reservoir property fields for a given fluvial scenario, not to the scenarios. In other words, the channel architecture—characterized by discrete facies—remains unchanged in ESMDA; only the internal property variations within the sand facies are adjusted.

As an extension of the ensemble smoother, ESMDA addresses nonlinearity in the model-data relationship by updating ensemble re-

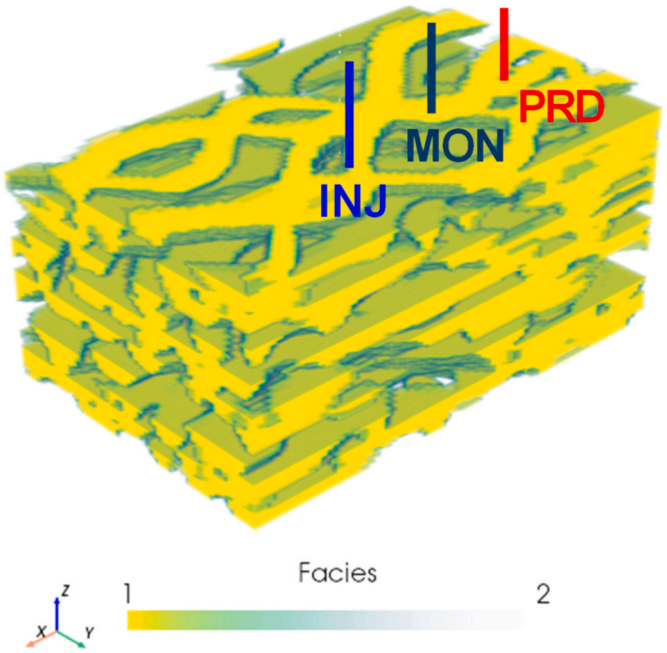

Fig. 5. 3D view of the reference scenario built with layer templates of mid-sinuosity channel belts, with channel widths ranging from 200 to 500 m, and NTG varying between 20% and 80%. In the visualization, the yellow regions represent the sand facies, while mudstone facies are shown as transparent (1 = sand, 2 = mudstone). The three lines indicate the injector, monitoring borehole, and producer. The reference scenario is the 'truth' reservoir architecture, and the channel sands contain heterogeneous petrophysical properties as well. (For interpretation of the references to colour in this figure legend, the reader is referred to the Web version of this article.)

alizations of one specific scenario over multiple assimilation steps using observed data. It introduces a set of inflation factors, applied to the observation covariance matrix, to control the size of updates at each iteration. This reduces the risk of overfitting and preserves ensemble diversity in property distributions. For each single geological scenario, the ESMDA process can be summarized in the following steps, as shown in Fig. 4 (Emerick and Reynolds, 2013).

1. Generate 100 prior realizations with heterogeneous properties for the single scenario. The ensemble size *Ne* is set to 100 and defined as

$$\mathbf{M} = [\mathbf{m}_1, \mathbf{m}_2, \ldots, \mathbf{m}_i, \ldots \mathbf{m}_{Ne}], \tag{7}$$

where $\mathbf{M}$ refers to the porosity in all grid cells that contain the sand facies, $\mathbf{m}_i = [\boldsymbol{\phi}]_i$.

2. Define key parameters in ESMDA. Set the number of iterations *Na*, and inflation factors α_l. l from 1 to N_a. Here, $\boldsymbol{\alpha} = [\alpha_1, \alpha_2, \ldots, \alpha_{Na}]$ is applied to measurement error covariance. The factors should satisfy the requirements of $\sum_{l=1}^{Na} \frac{1}{\alpha_l} = 1$.
3. For all realizations, solve the mass and energy conservation equations (2) and (3) from time zero until 50 years, and obtain predictions at measurement locations across all time steps

$$\mathbf{d}_i^l = G(\mathbf{m}_i^l), \tag{8}$$

where $\mathbf{m}_i^l$ represents the porosity and permeability fields for the i-th member at iteration l. $G(\mathbf{x})$ is a forward model.

4. Compute the covariance matrix as follows

$$\mathbf{C_{YD}} = \frac{1}{N_e - 1} \sum_{i=1}^{N_e} \left(\mathbf{m}_i^l - \overline{\mathbf{m}^l}\right)\left(\mathbf{d}_i^l - \overline{\mathbf{d}^l}\right)^T, \tag{9}$$

$$\mathbf{C_{DD}} = \frac{1}{N_e - 1} \sum_{i=1}^{N_e} \left(\mathbf{d}_i^l - \overline{\mathbf{d}^l}\right)\left(\mathbf{d}_i^l - \overline{\mathbf{d}^l}\right)^T, \tag{10}$$

where $\mathbf{C_{YD}}$ means the cross-covariance matrix between the model prediction and model parameters. $\mathbf{C_{DD}}$ means the covariance matrix of predicted data. For $l = 1$, $\mathbf{m}^1$ and $\mathbf{d}^1$ represent the prior parameters and prior predictions. For $l > 1$, they correspond to posterior parameters and updated predictions from the previous iteration. For each ensemble member, perturb the measurement vector using $\mathbf{d}_{uc} = \mathbf{d}_{obs} + \sqrt{\alpha_l}\mathbf{C_D}^{1/2}\mathbf{z_d}$, where $\mathbf{z_d} \sim \mathcal{N}(0, \mathbf{I}_{Nd})$, N_d is the total number of measurements assimilated, $\mathbf{d}_{obs}$ identifies the true observations, and $\mathbf{C_D}$ is the measurement error covariance matrix.

5. Update the parameter ensemble for the next iteration l+1 using

$$\mathbf{m}_i^{l+1} = \mathbf{m}_i^l + \mathbf{C_{YD}}(\mathbf{C_{DD}} + \alpha_l \mathbf{C_D})^{-1}\left(\mathbf{d}_{uc,i} - \mathbf{d}_i^l\right), i = 1, 2, \ldots, N_e. \tag{11}$$

6. Repeat steps 3 to 5 until the maximum number of iterations N_a is reached.

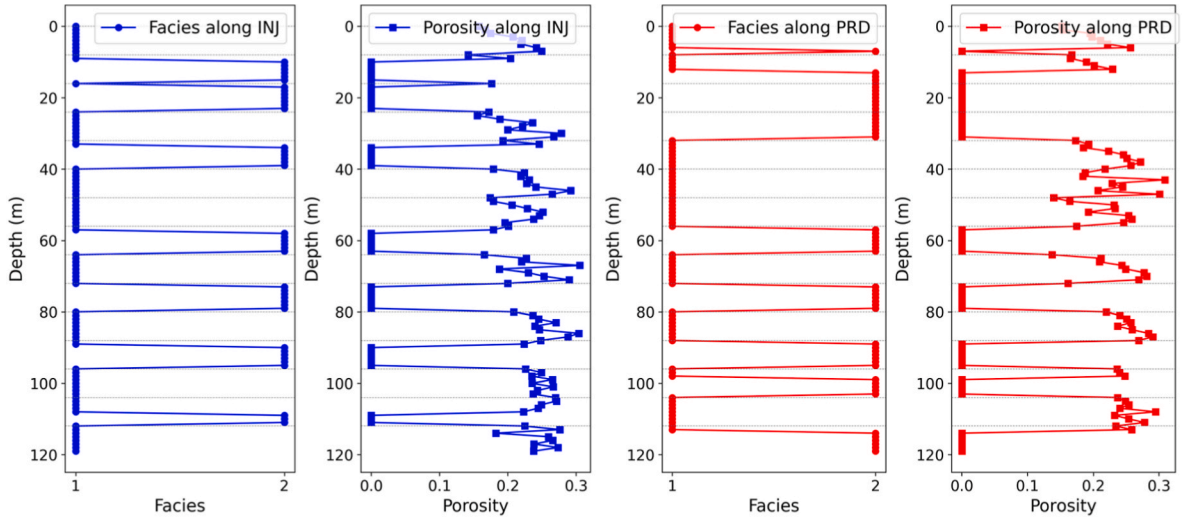

Fig. 6. Synthetic facies and porosity profiles along the injection well (blue) and production well (red) obtained from the reference model (Fig. 5). (For interpretation of the references to colour in this figure legend, the reader is referred to the Web version of this article.)

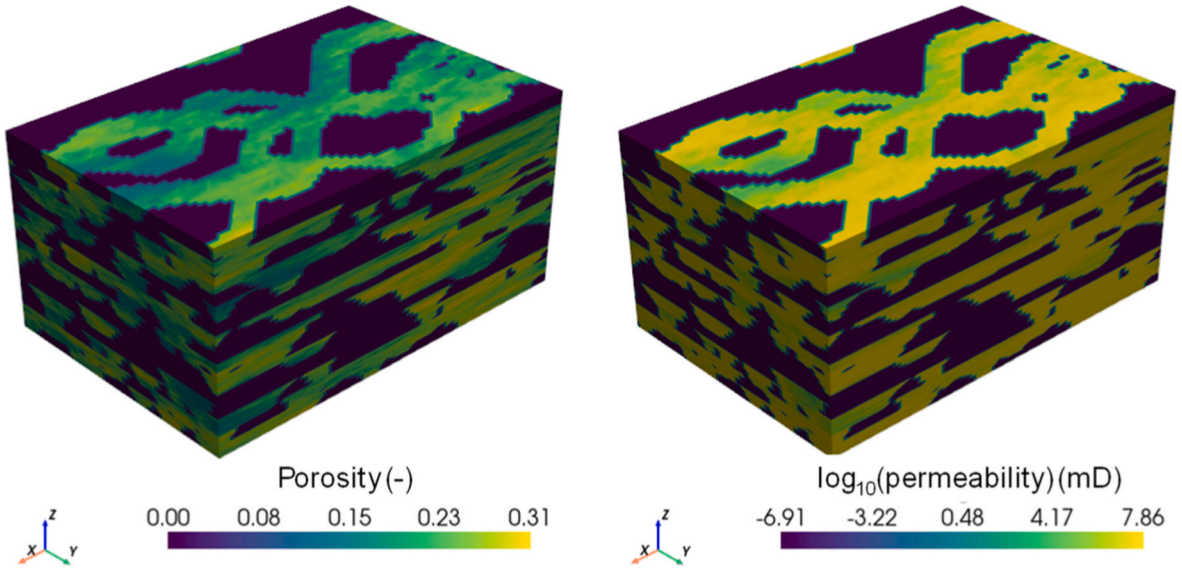

Fig. 7. The porosity (left) and permeability (right) distribution for the reference model that represents the 'truth' case. Production data for subsequent data assimilation are simulated for this 'truth' case. Model dimensions are 3000 m by 2000 m by 120 m.

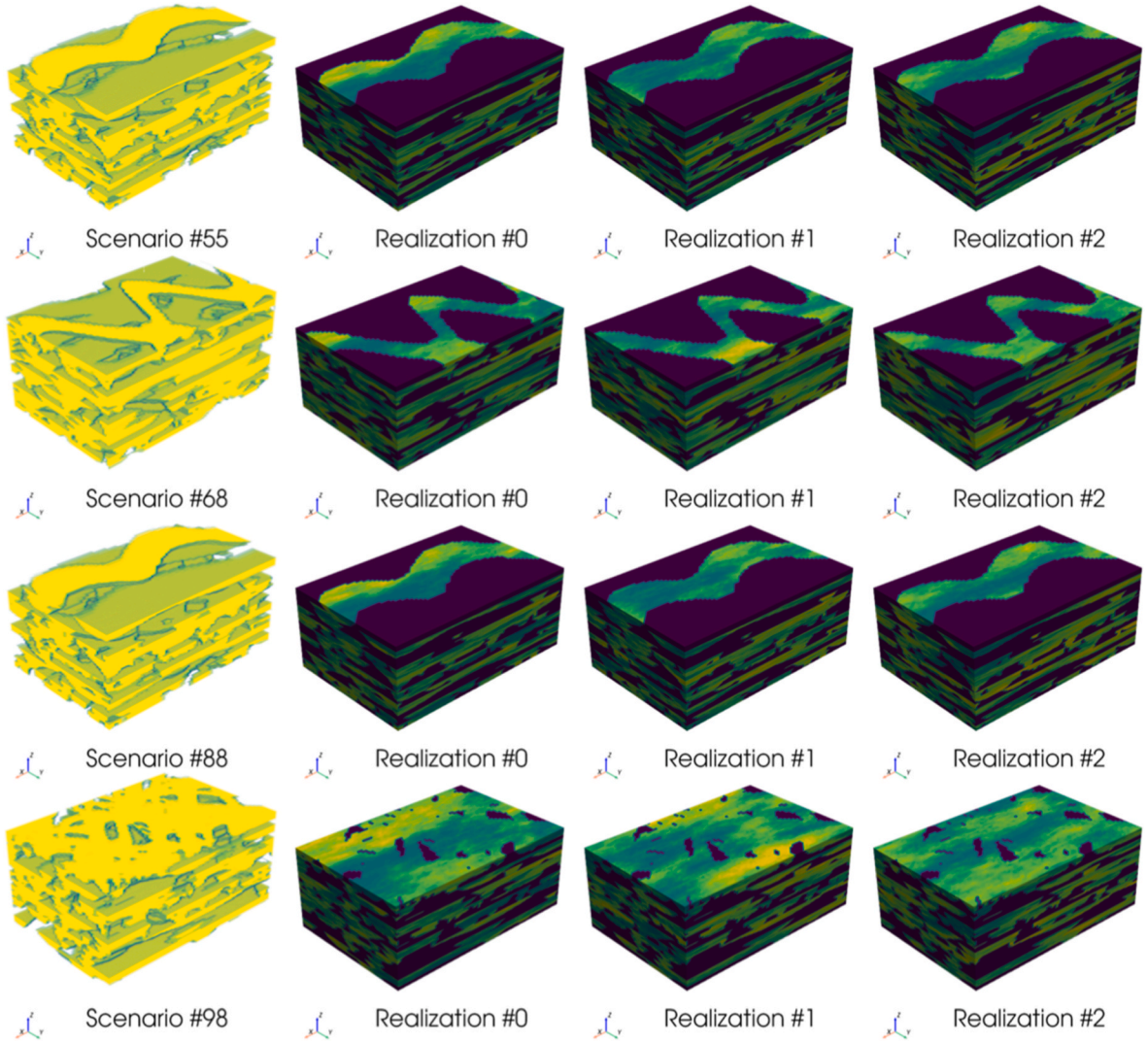

Fig. 8. Four examples of geological scenarios that illustrate differences in reservoir architecture but honor the facies profiles depicted in Fig. 6 (first column). Columns 2 to 4 show three examples of the equiprobable realizations of the porosity distribution for the given scenario.

Table 2
Numerical simulation parameters for the doublet geothermal system (Wang et al., 2021).

Parameters	Values
Reservoir dimensions	3000 m × 2000 m × 120 m
Injection-production spacing	1200 m
Well length	120 m
nx, ny, nz	75, 50, 120
dx, dy, dz	40 m, 40 m, 1 m
Porosity and k_h in sand facies	Homogeneous situation: 0.225 and 1500 mD Heterogeneous situation: see Figs. 7 and 8 and Equation (1)
Porosity and k_h in mudstone facies	0.0001 and 0.001 mD in mudstones
k_v/k_h	0.1
Initial reservoir pressure and temperature	200 bar and 353.15 K
Thermal conductivity	3.0 W/m/K for the sand bodies, 2.2 W/m/K for the mudstones
Volumetric heat capacity	2450 kJ/m^3/K for the sand bodies, 2300 kJ/m^3/K for the mudstones
Injection/production rate	10,000 m^3/day
Injection temperature	298.15 K

After the final iteration, the production curves are reproduced. Root mean square error (*RMSE*) and ensemble spread (*ES*) of porosity and production predictions are calculated to evaluate the data assimilation performance. In this study, production predictions specifically refer to the temporal temperature and pressure profiles along the wells. *RMSE* quantifies the ensemble error compared to the reference values. A lower *RMSE* indicates better data assimilation performance

$$RMSE = \sqrt{\frac{1}{N}\sum_{i=1}^{N}(S_i - M_i)^2}, \tag{12}$$

where S_i is the estimated value and M_i is the true value, and N is the total number of parameters. *ES* measures the average variability of individual ensemble members relative to the ensemble mean, reflecting a measure of range in the updated results. It is defined as

$$ES = \sqrt{\frac{1}{N}\sum_{i=1}^{N}(S_i - \overline{S}_i)^2}. \tag{13}$$

A lower *ES* indicates that the updated results are more centralized with reduced variability. A faster decrease in *ES* with iterations suggests a quicker convergence of the data assimilation process.

ESMDA is then applied for multiple scenarios, which are rapidly created through the aforementioned scenario-based geological modeling. Fig. 4 presents the scenario-based ESMDA framework that is carried out individually for the different fluvial geological scenarios. In this study, a total of 100 prior scenarios are generated, each representing a distinct reservoir architecture that is fully constrained by the same reference facies data along the well paths. For each scenario, an ensemble of 100 realizations is generated using geostatistical methods to model the porosity and permeability distributions. This means that there are 10,000 individual models in total. However, ESMDA is not applied to every scenario due to the significant computation load. Instead, we select a subset of scenarios for data assimilation based on 2 criteria: (1) the *RMSE* of simulated temperature and pressure profiles along the wells from prior scenarios — where uniform porosity and permeability are assigned to the sand facies in selection phase — with those of the reference scenario (as detailed in Section 3.2.3), and (2) the difference facies relative to the reference scenario, calculated as the root-mean-square deviation of facies values across the grid (as described in Section 3.3.2). During the initial screening stage, scenarios with both high and low *RMSE* values of simulation results, as well as high and low facies differences, are selected to form a representative subset. ESMDA is performed for the selected scenarios, and the prediction errors of posterior ensemble realizations for each scenario are compared with reference data. The reference 'observed' data used for all data assimilation are derived from the reference, or 'truth', case. Scenarios with higher *RMSE* of posterior simulations are identified as those that are less likely to represent the subsurface geology, i.e. are falsified, because the simulated production behavior disagrees with the reference observations. Conversely, scenarios with lower *RMSE* yield flow responses more consistent with the observed data of the reference 'truth' model and are retained as the plausible scenarios. It is important to note that ESMDA is designed for Gaussian distributed parameters. As noted above, the porosity and permeability fields within the channel sand facies are

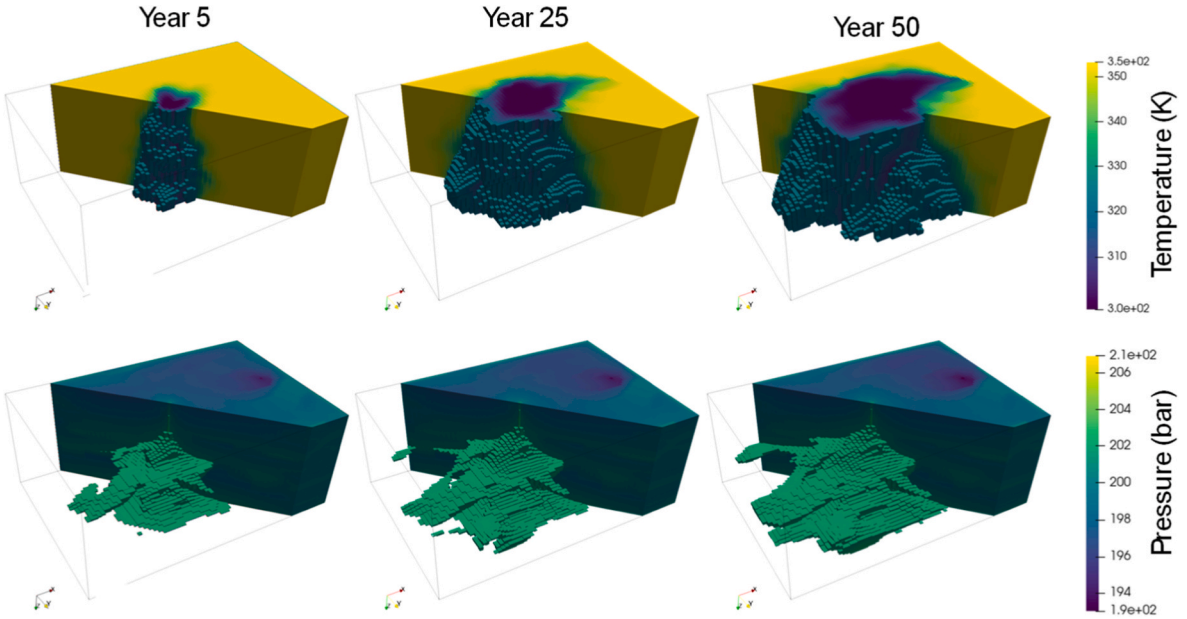

Fig. 9. Spatial view of temperature (upper row) and pressure (lower row) distributions after 5, 25, and 50 years of production for the reference case (from left to right). Cold zones and high-pressure zones are highlighted using the thresholds for temperature below 323 K and pressure above 202 bar.

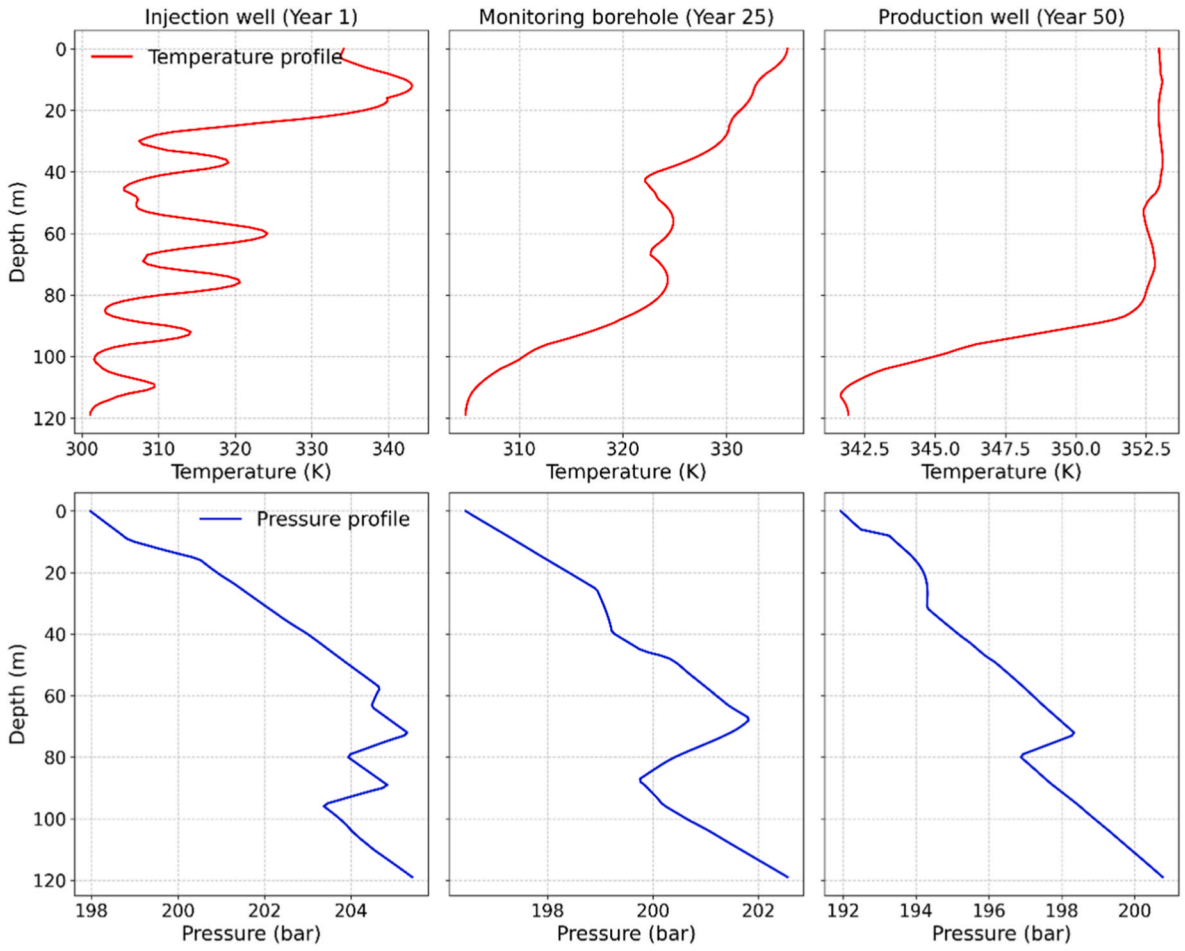

Fig. 10. Simulated temperature and pressure profiles as a function of depth at the injector, monitoring borehole, and producer, after 1, 25, and 50 years of production, respectively (from left to right) for the reference case.

generated using facies-controlled SGS, which follows a Gaussian distribution. ESMDA only updates the channel porosities. Facies and channel geometries are fixed during the assimilation process, meaning that the reservoir architecture is not updated.

3. Results

3.1. Geological models

3.1.1. Construction for reference scenario

As real production data from the Delft Campus geothermal field is not yet available, a synthetic reference scenario is constructed and considered to be the 'truth' scenario. It defines the 'truth' reservoir architecture with specific channel geometry, connectivity, etc. To differentiate the reference scenario from subsequent scenarios, key channel features are defined within a narrower range than those presented in Table 1. Channel width ranges from 200 to 500 m. The channels have moderate sinuosity. The NTG of a layer template varies from 20% to 80%. Fifteen cropped sub-regions are randomly extracted from the layer template library discussed in section 2 and stacked with 2 m overlaps. The reference scenario has dimensions of 3 km × 2 km × 120 m (Fig. 5).

The facies profiles along the injection and production wells are extracted from the reference scenario (Fig. 5), and the corresponding porosity profiles are synthetically assigned based on the facies along the well paths. These profiles are considered as interpreted well logs (Fig. 6) that must be honored when creating other models. SGS is then employed to model the porosity distributions within the sand facies across the entire reservoir, conditioned to the porosity profiles. The porosity-permeability relationship (Equation (1)) is used to calculate the permeability in the sand facies. Mudstone facies are assumed to be impermeable and hardly contribute to reservoir flow. Since the performance of geothermal systems was demonstrated to be largely insensitive to property variations in mudstones (Tas et al., 2025), the porosity and permeability for the mudstone facies are assumed to be uniform. Fig. 7 illustrates one representative property distribution for the reference scenario, which serves as the 'truth' case for subsequent uncertainty quantification and data assimilation in this study.

3.1.2. Construction for multiple scenarios

Using the facies profiles in Fig. 6 as constraints, 100 geological scenarios are created by recombining the cropped sub-regions of the different layer templates generated in RRM; each scenario honors these facies profiles but has very different reservoir architectures in terms of the 3D channel geometry and connectivity. Fig. 8 presents four example scenarios. Porosity and permeability distributions are then modelled for the sand facies using SGS as described above, while the properties for the mud facies have a uniform value as for the reference case. An ensemble of 100 equiprobable realizations for the properties of the sand facies is generated for each scenario. Fig. 8 shows the first 3 realizations for the corresponding scenarios. Different scenarios represent variations in reservoir architecture, i.e., channel geometry, connectivity, and stacking patterns. The final ensemble of reservoir models, comprising 100 scenarios with 100 realizations each, serves as inputs for geothermal reservoir simulations to evaluate how the different reservoir architectures (i.e., scenarios) and property distributions (i.e., porosity and permeability distributions) influence production performance forecasts.

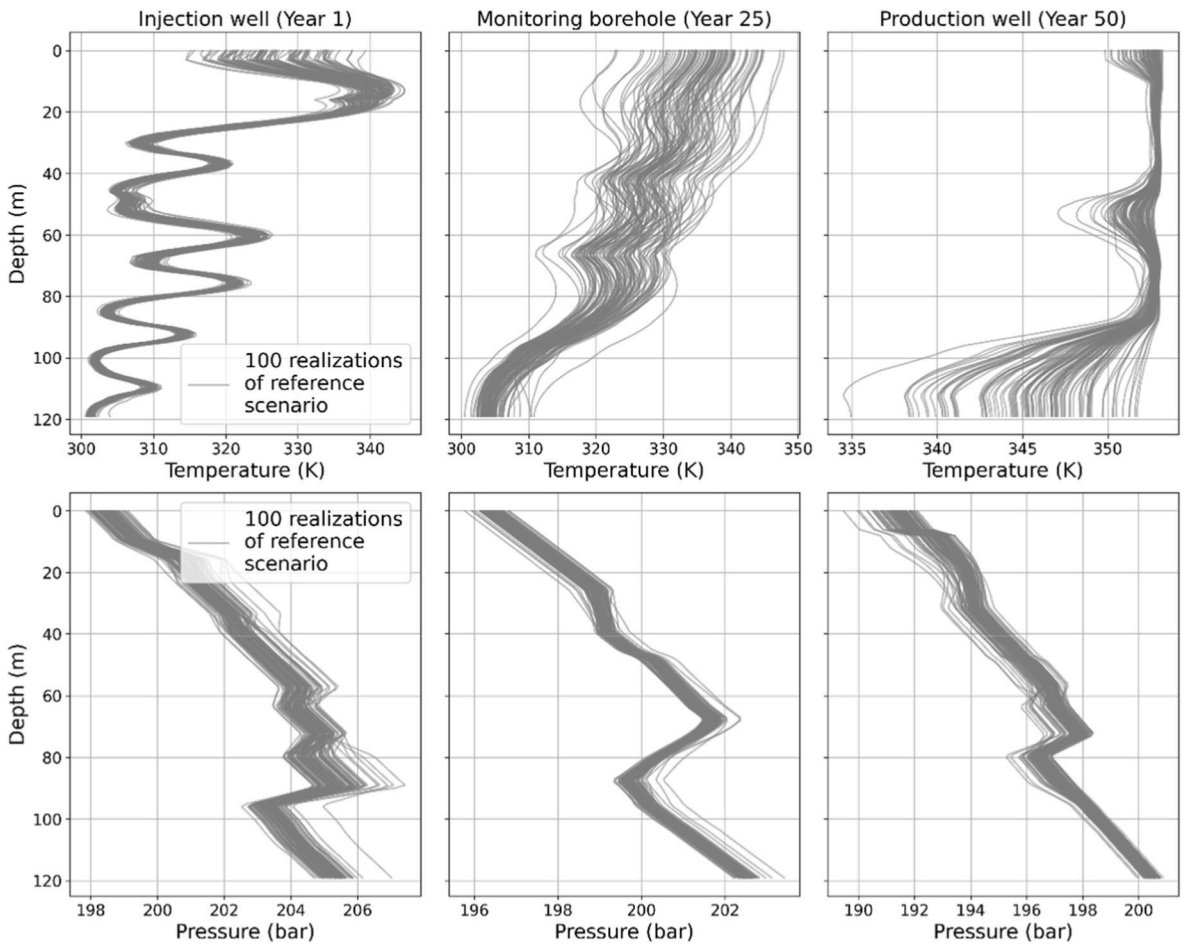

Fig. 11. Temperature and pressure profiles as a function of depth for the injector, monitoring borehole, and producer, after 1, 25 and 50 years of production, respectively (from left to right). Thin grey lines show the predictions for 100 equiprobable realizations of the reference scenario.

3.2. Geothermal reservoir simulation

The geothermal system considered is a typical doublet, with a producer well and an injector, with flow considered in the sedimentary system (Fig. 5). A less typical monitoring borehole is also considered in between the two wells, to investigate the impact of collecting additional reservoir information. There are plans to drill such a monitoring borehole at the Delft campus geothermal project as part of the EPOS-eNLarge project (https://epos-nl.nl/enlarge/). In this subsection, modeling parameters for all simulations are introduced first. Then, the results of the heat and fluid flow simulations for the 'truth' case are presented, including the spatial temperature and pressure distributions as well as the temporal evolution of the temperature and pressure profiles along the injection well, monitoring borehole, and production well. Finally, to assess the variability of production data, two situations are considered: 100 equiprobable realizations of the reference scenario are simulated to evaluate the impact of uncertain porosity and permeability distributions; 100 geological scenarios with uniform property values in the sand facies are simulated to assess the effects of variable reservoir architectures.

3.2.1. Model parameters

Table 2 summarizes the key parameters for the numerical simulations of heat and fluid flow in the reservoir. Inspired by the Delft campus geothermal project, we construct the reservoir model to approximate this specific geothermal doublet ()(Song et al., 2025). The reservoir is located at a depth of 2000 m, with dimensions of 3000 m $\times$ 2000 m $\times$ 120 m. The initial reservoir temperature is 353.15 K, and the initial pressure of 200 bar. Porosity and permeability have uniform values of 0.01% and 0.001 mD for the mudstone facies, respectively. The porosity distribution in the sand facies is modelled using SGS as discussed above. The rock thermal conductivity and heat capacity are 3.0 W/m/K and 2450 kJ/m^3/K for the mudstone, respectively, and 2.2 W/m/K and 2300 kJ/m^3/K for the sand facies, respectively. The reservoir is considered to contain water without any dissolved salts or gases. We assume no interactions, chemically or mechanically, between the geothermal water and the reservoir itself. Cold water is injected at the injection well and hot water is produced from the production well. The injection and production rate is 10,000 m^3/day, and the injection temperature is constant at 298.15 K. The distance between the injector and producer in the reservoir is 1200 m, with a monitoring borehole located halfway between them (Fig. 5). All wells are vertical in the reservoir and perforated over the entire 120 m reservoir interval. Vertical model boundaries are open to flow to mimic an infinitely large reservoir. Horizontal model boundaries are closed to flow, and there is no thermal recharge from an overburden or underburden. We note that this is a simplification, but the modelling concept presented here can be readily extended to account for more complex boundary conditions. We assume 50 years of production. The model is discretized into 40 m $\times$ 40 m $\times$ 1 m cells, resulting in a grid size of 75 $\times$ 50 $\times$ 120 with a total of 450,000 cells. We record temperature and pressure along the entire injector, monitoring borehole, and producer for each time step during the simulation. The resulting observations, i.e. temporal evolution of temperature and pressure along the wells, will be used for the data assimilation step.

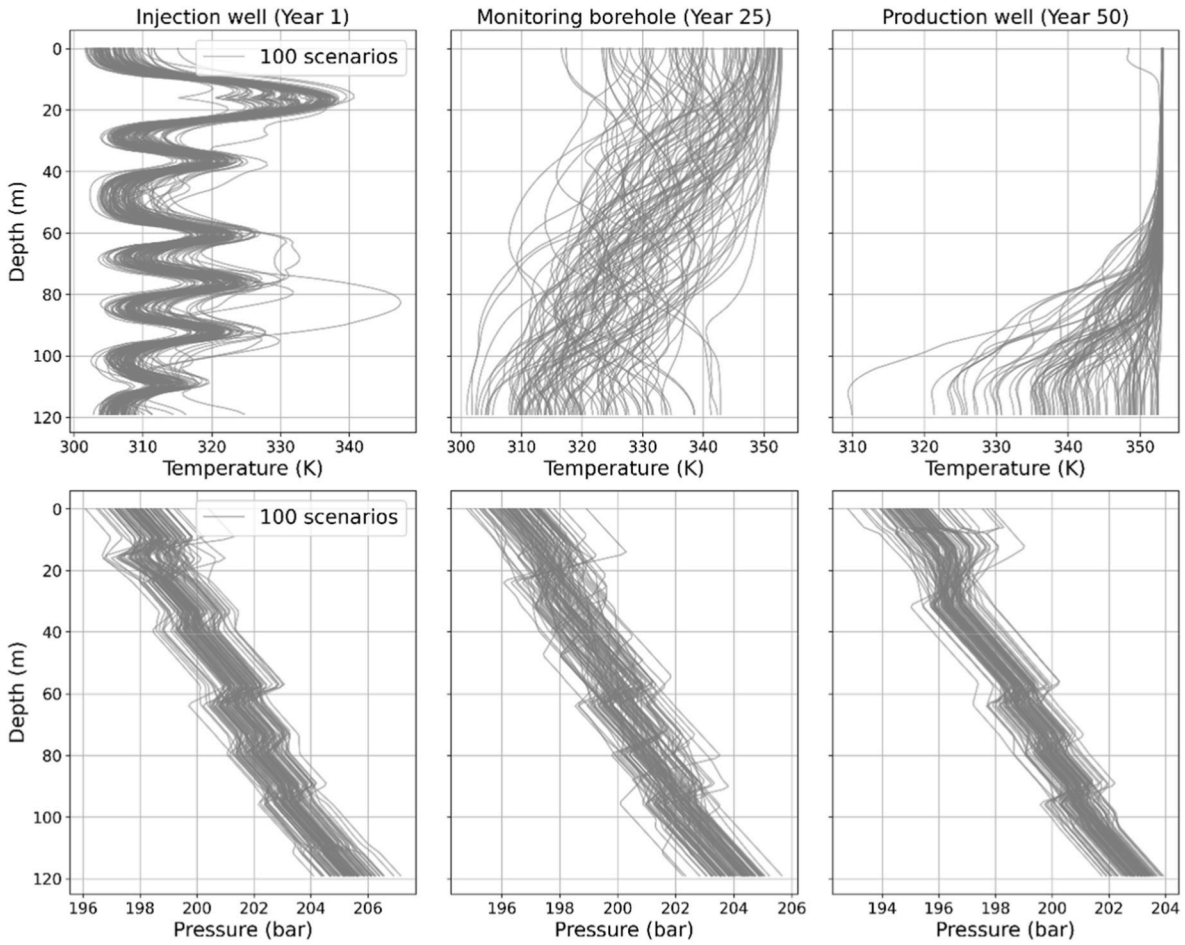

Fig. 12. Temperature and pressure profiles recorded as a function of depth for the injection well, monitoring borehole, and production well, after 1, 25, 50 years of production (from left to right) for geological scenarios with homogeneous channel properties. Grey lines represent the results for 100 prior scenarios with uniform channel properties.

Table 3
ESMDA parameters.

Parameters	Values
Number of iterations	4
Ensemble size	100
Unknown parameter	Porosity
Size of unknown parameter	450,000
Inflation factor	[9.43, 7, 4, 2]
Observations	Temporal evolution of temperature and pressure profiles observed along the injection, monitoring borehole, and production well simulated for the 'truth' case
Observation error	1 K for temperature and 2 bar for pressure
Evaluation metrics	*RMSE* and *ES*
lower and upper limits of porosity	0.13 to 0.31

3.2.2. Simulation for reference case

Fig. 9 presents the simulated spatial temperature and pressure distribution for the reference case (Fig. 7). Temperature and pressure distributions clearly show the heterogeneous nature of the flow field, controlled by the reservoir architecture, i.e. the 3D channel geometry and connectivity. The pressure distribution is influenced by the reservoir architecture and the corresponding permeability field, while the temperature field is also impacted by thermal conduction and convection. Because the time-scales of pressure diffusion are very short, the pressure field is established very quickly and remains relatively constant over time. In contrast, the temperature distribution continues to evolve as cold water moves from the injector to the producer and thermal conduction smears out temperature gradients.

Fig. 10 illustrates the simulated temperature and pressure profiles along three wells at different times for the reference case. The temperature profiles are smoother than pressure profiles as pressure is more sensitive to the permeability contrast, while temperature profiles are also 'smeared' due to thermal conduction. However, both types of profiles display distinct changes in curvature and inflection points as a function of depth that correspond to different reservoir layers. For the temperature profiles, regions with low temperatures indicate prominent heat convection and hence faster advance of the cold front, indicating the presence of connected sand facies with higher permeability that facilitate rapid cooling. Conversely, higher temperatures suggest limited convective heat transport, indicating the presence of either unconnected sands or low-permeability mud facies. Initially, the temperature profile along the injection well shows significant changes as the cold water begins to invade the formation. The temperature profiles observed at the monitoring borehole provide the most information throughout the production period. This is because they can capture the arrival and passing of the cold front. At the production well, the temperature profiles offer limited information until the cold front reaches the well. As noted above, pressure equilibrates more rapidly than temperature in the reservoir. Pressure profiles observed along the wells primarily reveal information about the layering in the reservoir. Regions where the observed pressure in the profile is close to the initial reservoir pressure indicate the presence of low-permeability mud facies, whereas regions

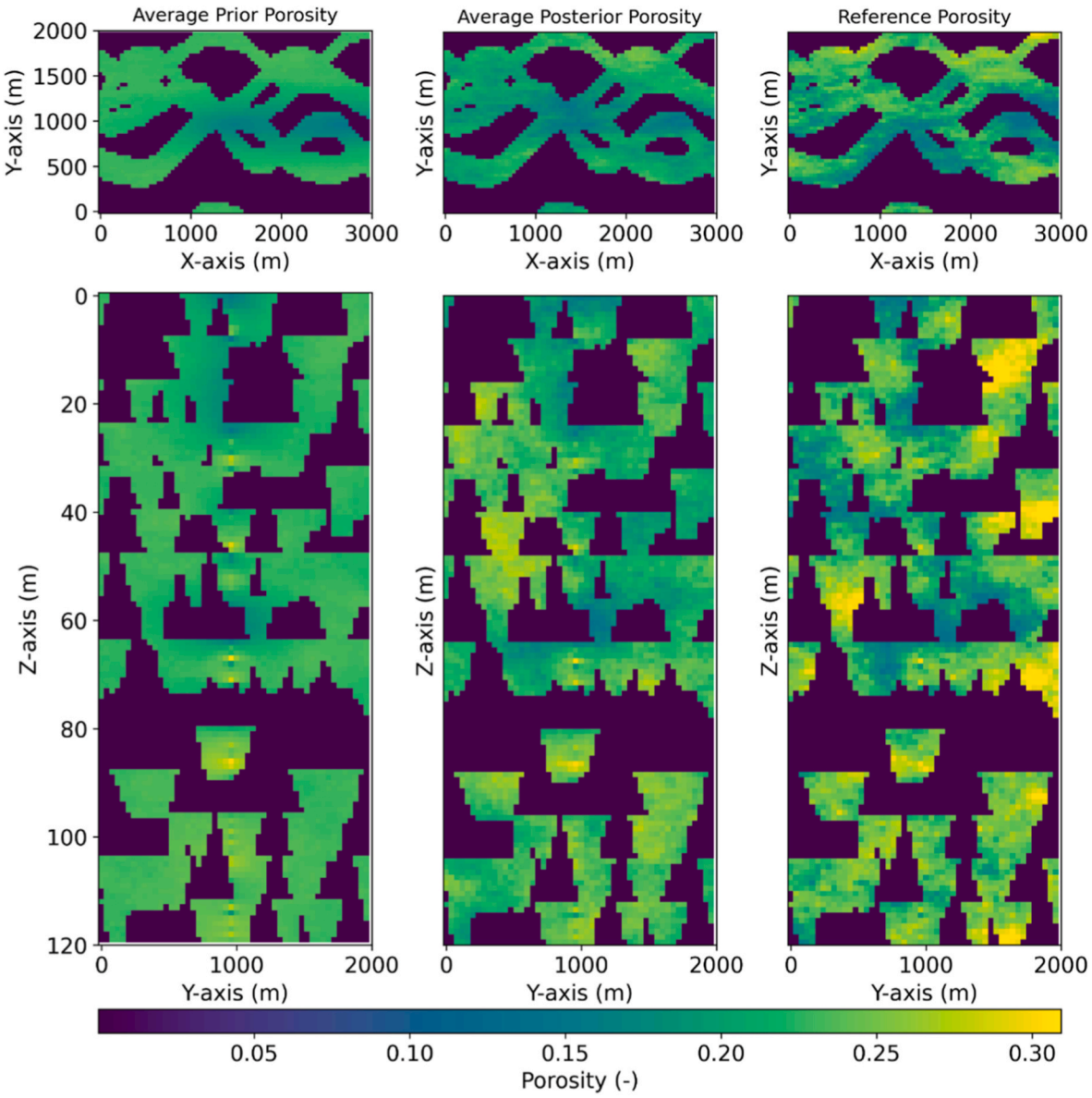

Fig. 13. Map view of the areal averaged porosity distribution for the prior and posterior ensembles and the distribution for the 'truth' case. The first row shows the map view at the top of the reservoir, and the second row displays the cross section at $x = 1500$ m.

where the pressure has decreased below the initial reservoir pressure indicate the presence of connected sand facies. Therefore, inflection points in the pressure and temperature profiles can be used to assess layer information and reservoir connectivity. Consequently, temperature and pressure profiles observed along three wells are incorporated as observations in the data assimilation process.

3.2.3. *Uncertainty analysis for the production data*

To quantify the uncertainty in the simulated production data arising from the uncertainty in the porosity and permeability distributions, heat and fluid flow are simulated for each of the 100 equiprobable realizations of the reference case. Fig. 11 shows the resulting temperature and pressure profiles for three wells for each realization. The difference in these profiles is directly related to the variability, i.e. uncertainty, in the petrophysical properties. Temperature profiles exhibit greater variability than pressure profiles. At the monitoring borehole, the maximum difference in temperature profiles is up to 28.0 K after 25 years of production. The pressure profiles vary between 196 and 204 bar, with a maximum range of 1.2 bar.

Numerical simulations were also conducted for the 100 different scenarios considering uniform properties in sand facies to investigate the impact of uncertain reservoir architectures on production behavior. Fig. 12 shows the resulting temperature and pressure profiles along the three well paths. In contrast to the simulation results for the single reservoir scenario with equiprobable realizations of the petrophysical property distributions (Fig. 11), the temperature and pressure profiles show greater variability. The maximum differences in temperature and pressure profiles at the monitoring borehole are 41.8 K and 4.3 bar, respectively, after 25 years of production. After 50 years of production, these differences are 50.6 K and 4.4 bar. These differences indicate that uncertainty in reservoir architecture, i.e. variability in 3D channel geometry and channel connectivity, has a larger impact on production behavior than the variations in permeability and porosity distributions within the sand facies of the fluvial channels. Relying solely on the uncertainty of petrophysical property while keeping the reservoir architecture fixed, therefore, is unlikely to capture the full spectrum of geological uncertainty. Hence, for data assimilation, both aspects – uncertainties in channel geometry and connectivity as well as uncertainties

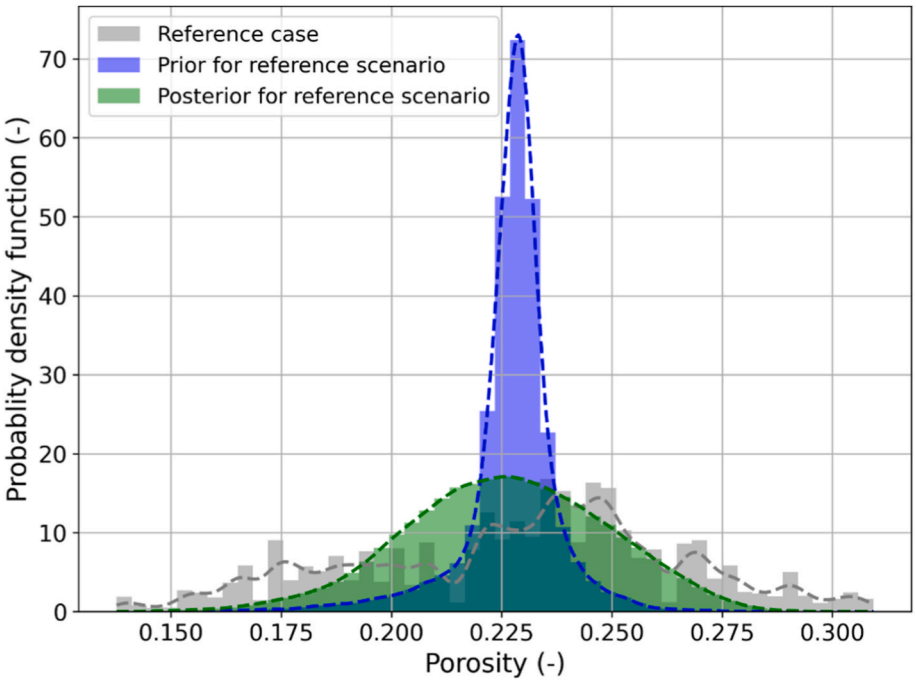

Fig. 14. PDFs of the average porosity in the sand facies for the prior (purple) and posterior (green) ensembles, and the PDF of the porosity in the sand facies for the 'truth' case (grey). Note that the (wider) variance of the posterior ensemble is in better agreement with the 'truth' case. (For interpretation of the references to colour in this figure legend, the reader is referred to the Web version of this article.)

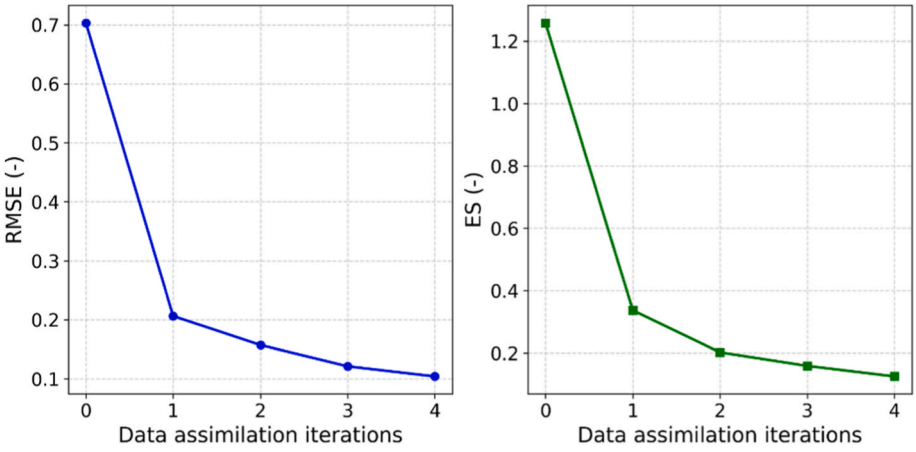

Fig. 15. Evolution of *RMSE* (left) and *ES* (right) for the temperature and pressure profiles for four iterations of data assimilation.

in porosity and permeability distribution – need to be considered.

3.3. Data assimilation

In this subsection, ESMDA is first applied to the reference scenario to refine the ensemble realizations and evaluate the performance of the algorithm. Then, scenario-based ESMDA is employed across multiple scenarios and identifies the more likely scenarios in comparison to the reference scenario. During ESMDA, only the properties within the channels of ensemble realizations are updated while the reservoir architecture remains unchanged.

3.3.1. Data assimilation for the reference scenario

Table 3 summarizes the ESMDA parameters. The observation data consist of the temporal evolution of the temperature and pressure profiles along the injector, monitoring borehole, and producer simulated for the 'truth' case. Observation errors are set at 1 K for temperature and 2 bar for pressure, based on typical monitoring equipment. Four iterations are performed with inflation factors. The ensemble contains 100 equiprobable realizations of porosity and permeability distributions, as discussed above.

Fig. 13 shows map views and cross sections that illustrate the areal average porosity distribution for the prior and posterior ensemble realizations, as well as the porosity distribution for the reference case. In the map view, a distinct low-porosity zone in the sand facies, parallel to the main channel direction, is evident in the posterior ensemble. This low-porosity zone is also apparent in the reference case. In the vertical cross section, the local porosity distribution in the vicinity of the wells ($y = 1000$ m) improves, i.e. is closer to the 'truth' case, after data assimilation. Fig. 14 demonstrates the probability density function (PDF) of the average channel sand porosity for the prior and posterior ensemble realizations, as well as the PDF for the porosity of the sand facies for the 'truth' case. The sand porosity in the prior and posterior ensembles follows Gaussian distributions, yet has pronounced

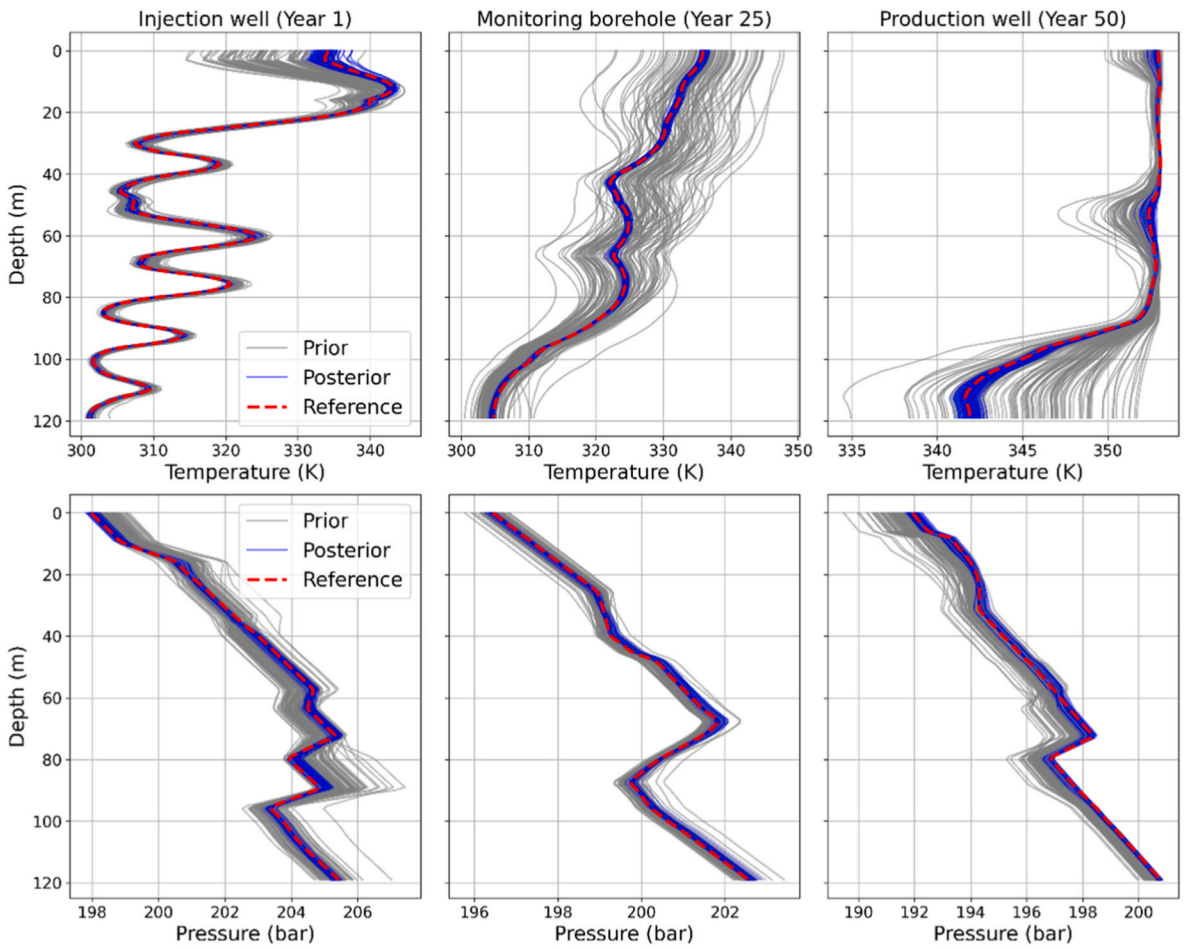

Fig. 16. Prior, posterior, and reference temperature and pressure profiles recorded as a function of depth for the injection well, monitoring borehole, and production well, after 1, 25, and 50 years of production, respectively (from left to right). The grey lines show the forecasts for the prior ensemble, the red line denotes the 'observed' data for the 'truth' case, and the blue lines are the predictions for the posterior ensemble after data assimilation. (For interpretation of the references to colour in this figure legend, the reader is referred to the Web version of this article.)

differences in variance. The variance of the posterior PDF is in better agreement with the PDF of the 'truth' case. Fig. 15 presents the *RMSE* and *ES* for the temperature and pressure profiles for four iterations of data assimilation. *RMSE* and *ES* decrease with each iteration, indicating convergence towards the true observations and a more reliable and better constrained production forecast.

Fig. 16 compares the prior predictions, posterior predictions, and reference data for the temperature and pressure profiles along the injector, monitoring borehole, and producer at different times. After data assimilation, the predictions for the posterior ensemble are in much better agreement with the 'observed' data from the 'truth' case. The variability of predictions for the posterior ensemble is also reduced, indicating that the overall uncertainty in production forecasts is much better constrained. Take the temperature and pressure profiles at the monitoring borehole after 25 years of production as an example: the average temperature range at any depth decreases from 19.5 K in the prior to 1.4 K in the posterior, while the average pressure range is reduced from 1.0 to 0.4 bar. These results confirm the feasibility of ESMDA in constraining production uncertainty in fluvial geothermal systems for a single geological scenario.

3.3.2. *Data assimilation for multiple scenarios*

Based on the results shown in Section 3.2.3, 18 out of the 100 individual geological scenarios representing the different reservoir architectures are selected for the scenario-based ESMDA procedure. We calculated the *RMSE* for the temporal evolution of the temperature and pressure profiles along three wells. The profiles were normalized separately, and a weighted sum of the two was used to obtain a single *RMSE* value. The three scenarios with the lowest *RMSE* are #53, #20, and #54, while those with the highest *RMSE* are #18, #27, and #64. To ensure the diversity of selected scenarios, we also calculated the facies difference relative to the reference geological model, defined as the square root of the sum of squared differences between grid-level facies values. While this metric does not capture architectural similarity such as connectivity, it helps identify scenarios with different facies distributions that may still lead to similar or divergent production responses. Since the true subsurface channel distribution is unknown, random selection is a valid approach. To facilitate a clear comparison with our defined 'truth' scenario (Fig. 5), we instead select scenarios based on their facies differences. The three scenarios with the lowest facies differences are #68, #88, and #72, while those with the highest differences are #49, #10, and #45. Scenarios #21, #9, #55, #91, #98 and #61 are also randomly selected for scenario-based ESMDA. These 18 scenarios are kept for data assimilation to evaluate the ability of scenario-based ESMDA to falsify scenarios. The reference case is still the same 'truth' case in Section 3.3.1. We will also compare the heterogeneity of these scenarios further below.

Take Scenario #68 as an example, an ensemble of 100 equiprobable realizations of heterogeneous porosity and permeability was generated using the same geostatistical procedure as for the reference scenario. Fig. 17 shows map views and cross sections that illustrate the areal average porosity distribution for the prior and posterior ensemble

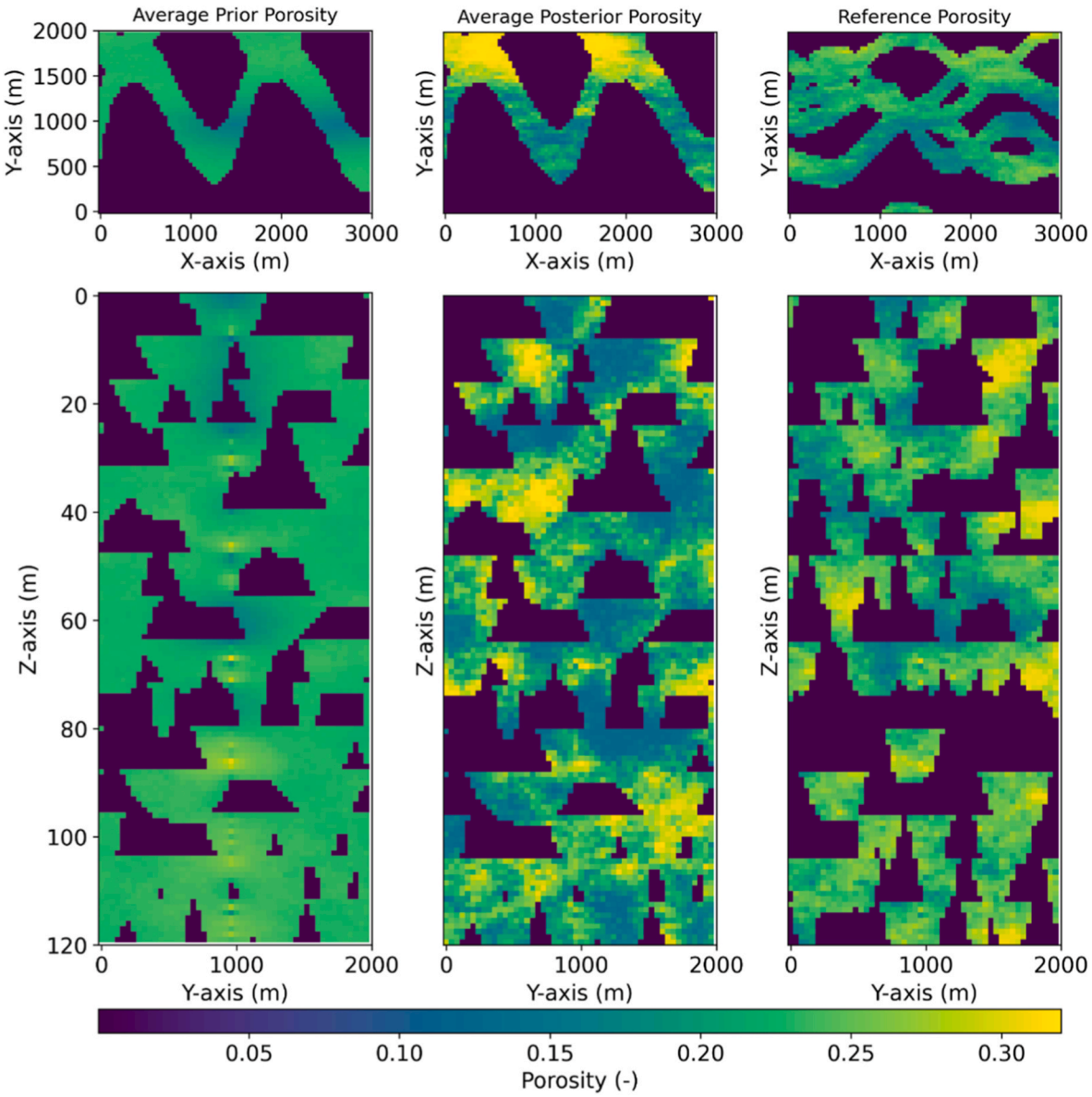

Fig. 17. Map view of the areal averaged porosity distribution for the prior and posterior ensembles of Scenario #68 and the distribution for the 'truth' case. The first row shows the map view at the top of the reservoir and the second row displays the cross section at x = 1500 m.

realizations of Scenario #68, as well as the porosity distribution for the 'truth' case. The posterior porosity of Scenario #68 exhibits spatial contrasts compared to the prior, with porosity values in some regions pushed toward the upper bound and others toward the lower bound. Fig. 18 presents the PDF of the average porosity and log-permeability for the sand facies for the prior and posterior ensembles of Scenario #68, and the PDF for the sand porosity and log-permeability for the reference case. The PDF for the porosity of the prior ensemble follows a Gaussian distribution. However, the PDF for the porosity of the posterior ensemble has a uniform distribution and deviates from the reference case; note that there are two small peaks in porosity near the lower and upper limits of the porosity distribution. The logarithmic permeability is computed from porosity based on Equation (1). The posterior log-permeability distribution deviates from the prior, becoming non-Gaussian, broader and flatter, with local density increases near the lower and upper limits. In cases where the reservoir architecture differs from the reference scenario, ESMDA pushes the values of porosity and permeability toward their limits defined in the model parameteriszation in order to compensate for structural mismatches and better reproduce the 'observed' data. Fig. 19 illustrates that *RMSE* and *ES* decrease over subsequent data assimilation iterations, indicating that the uncertainty in production forecasts becomes better constrained.

Fig. 20 compares the prior and posterior predictions of Scenario #68 with the 'observed' data of the truth case for the temperature and pressure profiles at the three wells. The posterior profiles align better with the 'observed' data than the prior. The variability of posterior forecasts is also constrained. Take the temperature and pressure profiles at the monitoring borehole after 25 years of production as an example: the temperature *RMSE* decreases from 8.1 K in the prior to 0.3 K in the posterior, while the pressure *RMSE* is constrained from 1.1 to 0.8 bar. Although Scenario #68 has a different reservoir architecture than the 'truth' case, the adjustments imply that the ensemble is compensating for structural mismatch by selectively enhancing and suppressing flow-capacity-related properties in different parts of the model domain. ESMDA may therefore yield good matches for the wrong reasons.

For comparison, the ESMDA results for Scenario #98 are presented in Fig. 21 and Fig. 22. The prior, posterior, and reference porosity and permeability distributions in the sand facies exhibit a truncated

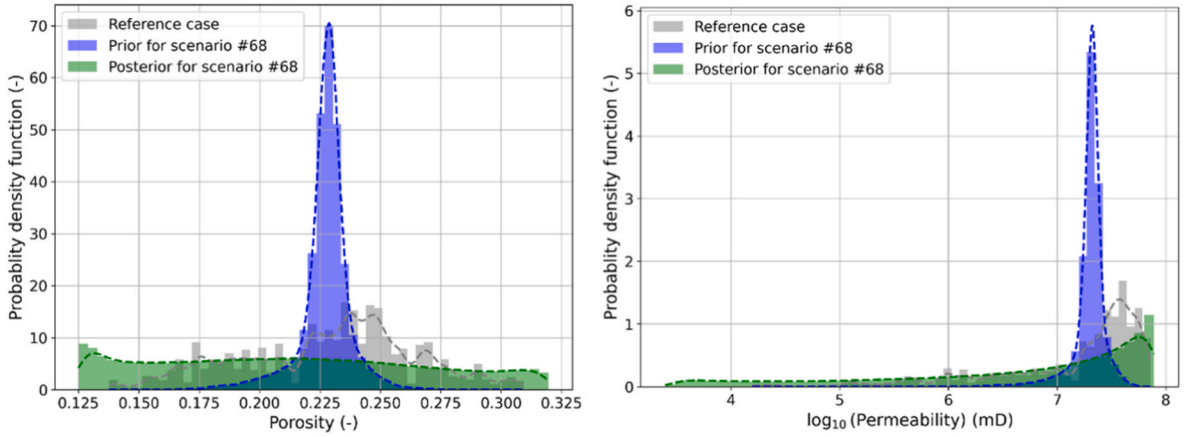

Fig. 18. PDFs of average sand porosity (left) and permeability (right) in the sand facies for the prior (purple) and posterior (green) ensembles of Scenario #68, and the PDF of the porosity and permeability in the sand facies for the 'truth' case (grey). Note that the distribution of the posterior PDF is non-Gaussian due to the different reservoir architecture from the 'truth' case. (For interpretation of the references to colour in this figure legend, the reader is referred to the Web version of this article.)

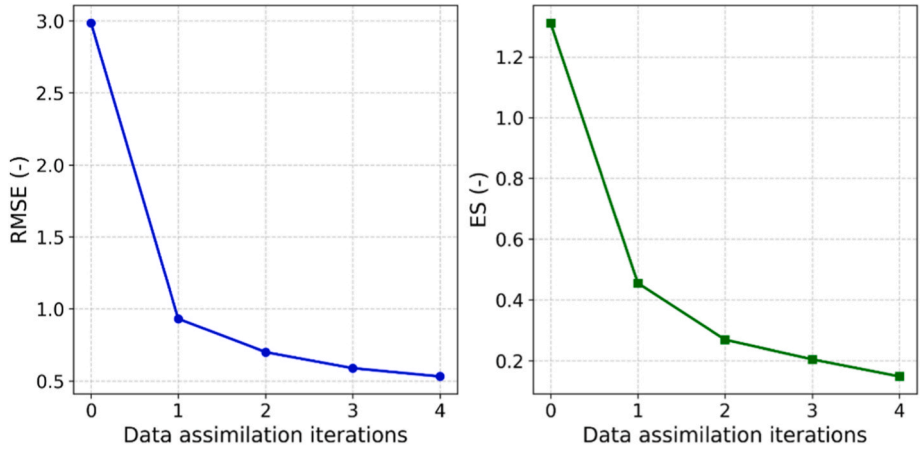

Fig. 19. Evolution of *RMSE* (left) and ES (right) for temperature and pressure profiles over four iterations of data assimilation for Scenario #68.

distribution, with most porosity and permeability values accumulated at the low and high endmember values (Fig. 21). This is because the channel distribution in Scenario #98 differs substantially from the reference scenario. To force the model prediction to be closer to the reference observations, ESMDA pushes the porosity and permeability for the sand facies towards the maximum and minimum allowable values to, leading to the apparent trunction. This behaviour indicates poor data assimilation results, which are demonstrated in Fig. 22. A similar phenomenon to Scenario #68 is observed, i.e. uncertainty in production forecasts is constrained as a result of data assimilation, yet mismatches of profiles between the posterior and the 'observed' data remain. The temperature and pressure profiles at the monitoring borehole after 25 years are used as an example: the temperature *RMSE* decreases from 6.5 K in the prior to 1.5 K in the posterior, while the pressure *RMSE* is constrained from 1.4 to 1.2 bar. The shifts and changes in the shape of the curves for Scenario #98 are more pronounced than those for Scenario #68. This indicates that Scenario #98 deviates more sigfinicantly from the reference behavior, both qualitatively and quantitatively. In contrast, Scenario #68 yields smaller *RMSE* values and better matches the observed data, suggesting it is more consistent with the true reservoir architecture, while Scenario #98 is less likely to represent the real reservoir architecture and hence can probably be falsified when compared to Scenario #68. The results also demonstrate the well-known fact that although ESMDA can adjust porosity and permeability in cases where a geological scenario is close to the real reservoir architecture, ESMDA in itself is not easy to deal with the larger uncertainties that arise when considering multiple geological scenarios that represent different reservoir architectures since these uncertainties of complex architectures is not easy to be parameterized. However, we can use this shortcoming to our advantage: If ESMDA yields porosity and permeability distributions that are either unrealistic and/or fail to yield a good agreement between observed data and simulated data for the posterior ensemble, then it is likely that a given geological scenario is not representative of the reservoir architecture and can hence be falsified. However, to use ESMDA in this way, it is crucial to consider and construct multiple geologically plausible scenarios as discussed here.

The well production response is not used in data assimilation and therefore serves as an independent benchmark for evaluating model performance. Fig. 23 illustrates the variations in production estimates for the posterior and prior ensembles of the reference scenario, Scenario #68, and Scenario #98. The posterior production curves of the reference scenario—which represents the 'truth' reservoir architecture—show the best match with the 'truth' production response. For Scenario #68, the production curves for the posterior ensemble contain the 'truth' production behavior. In contrast, the production forecasts for the posterior ensemble for Scenario #98 deviate significantly from the 'truth', indicating that Scenario #68 yields more reliable production forecasts than Scenario #98 because the reservoir architecture of Scenario #68 is closer to the real reservoir scenario.

To evaluate the performance of ESMDA across the eighteen reservoir

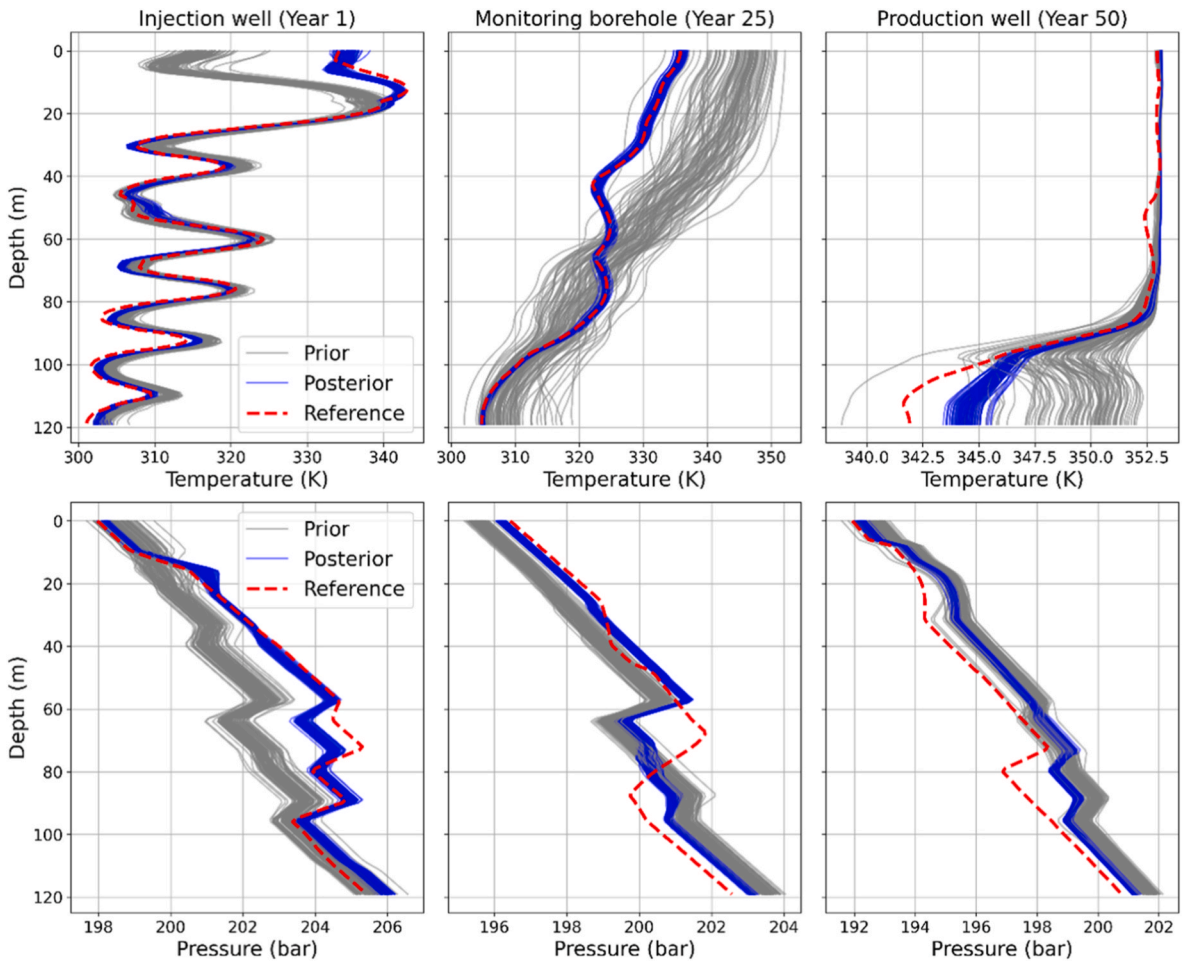

Fig. 20. Prior, posterior, and reference temperature and pressure profiles recorded as a function of depth for the injection well, monitoring borehole, and production well, after 1, 25, and 50 years of production, respectively(from left to right). The grey lines show the forecasts for the prior ensemble of Scenario #68, the red line denotes the 'observed' data for the 'truth' case, and the blue lines are the predictions for the posterior ensemble of Scenario #68 after data assimilation. (For interpretation of the references to colour in this figure legend, the reader is referred to the Web version of this article.)

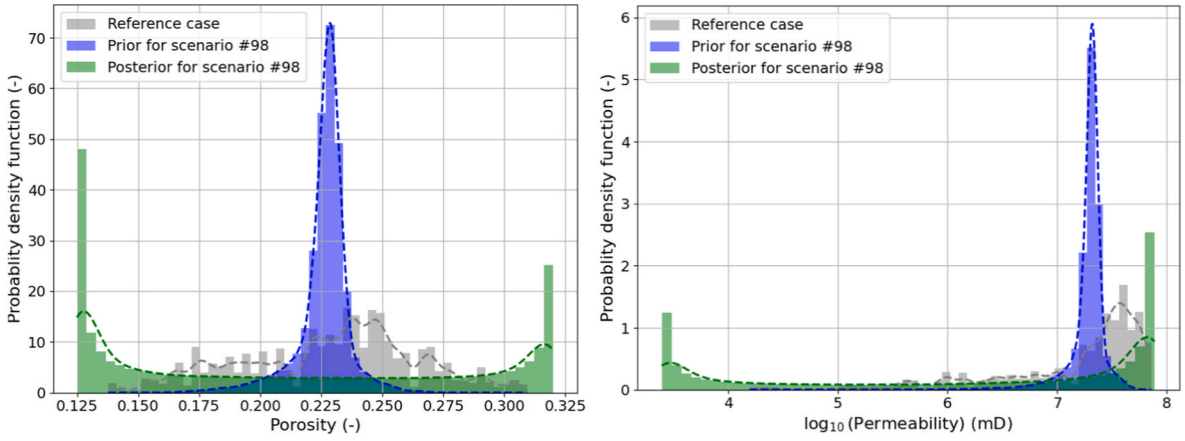

Fig. 21. PDFs of average sand porosity (left) and permeability (right) in the sand facies for the prior (purple) and posterior (green) ensembles of Scenario #98, and the PDF of the porosity and permeability in the sand facies for the 'truth' case (grey). Note that the distribution of the posterior PDF is non-Gaussian due to the different reservoir architecture from the 'truth' case. (For interpretation of the references to colour in this figure legend, the reader is referred to the Web version of this article.)

scenarios and the reference scenario corresponding to the 'truth' case, the normalized *RMSE* of the simulated temperature and pressure profiles along the three wells for the posterior ensemble for each scenario are compared (Fig. 24). The lowest *RMSE* values are observed for Scenarios #18, #49, #54, #55, #61, #64, #68, #72, #88, and #91. The *RMSE* for the production temperature and the pressure difference between injector and producer after 50 years are shown in Fig. 25. After data assimilation, most posterior results exhibit lower *RMSE* compared to the

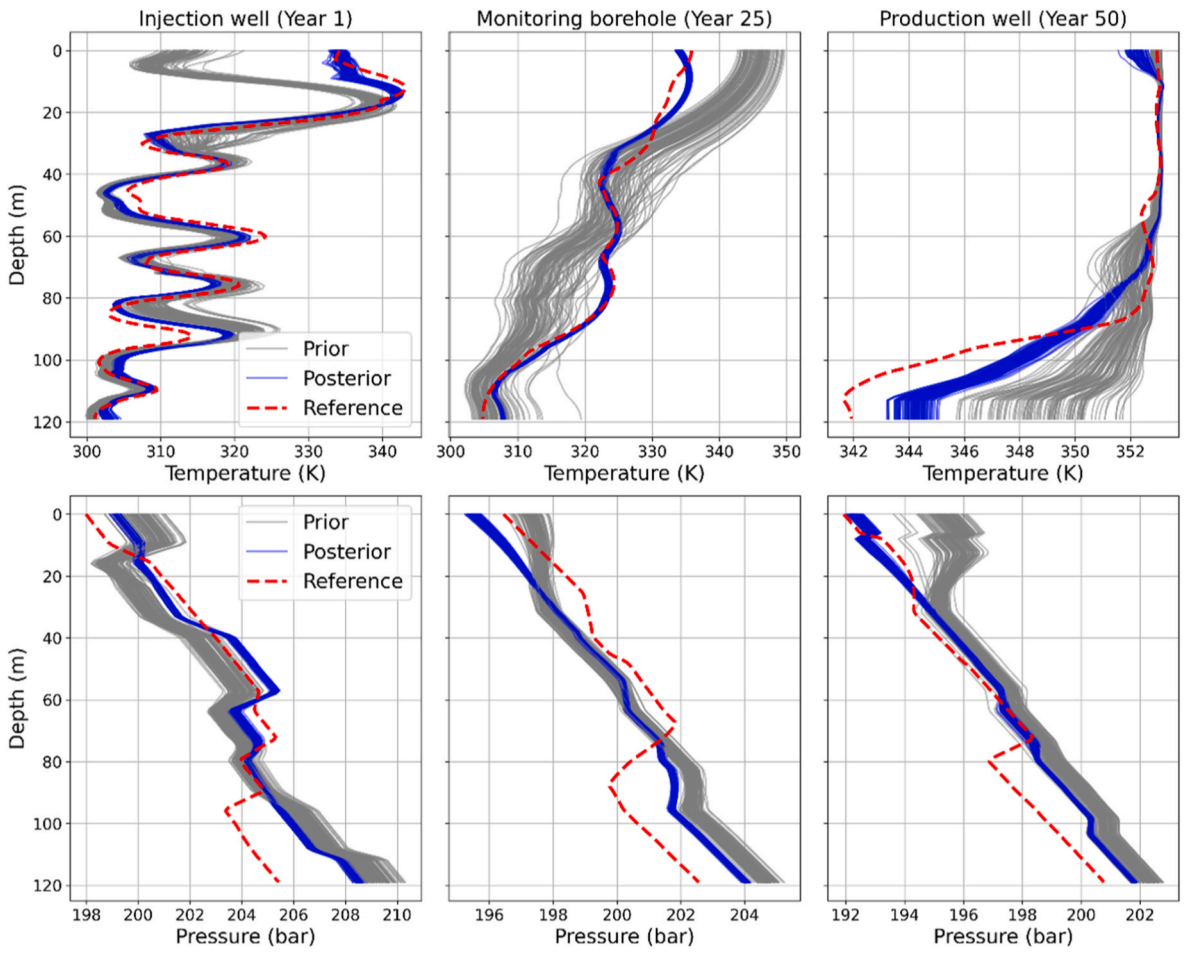

Fig. 22. Prior, posterior, and reference temperature and pressure profiles recorded as a function of depth for the injection well, monitoring borehole, and production well, after 1, 25, and 50 years of production, respectively(from left to right). The grey lines show the forecasts for the prior ensemble of Scenario #98, the red line denotes the 'observed' data for the 'truth' case, and the blue lines are the predictions for the posterior ensemble of Scenario #98 after data assimilation. (For interpretation of the references to colour in this figure legend, the reader is referred to the Web version of this article.)

prior results. Scenarios #18, #49, #54, #55, #61, #64, #68, #72, #88, and #91 exhibit lower *RMSE* for both production temperature and pressure difference (see also Fig. 23 for an example of the good agreement between simulated and 'truth' production temperature and pressure difference in Scenario #68). Considering the results in Fig. 24, these low *RMSE* errors imply that Scenarios #18, #49, #55, #61, #64, #68, #72, #88, and #91 are more likely to represent reservoir architectures that are good representations of the real reservoir architectures and should hence be considered further as plausible scenarios when estimating future production. In contrast, the other Scenarios #9, #10, #20, #21, #27, #53, #65, and #98 have high *RMSE* (see Fig. 23 for an example of the poor agreement between simulated and observed production temperature and pressure difference in Scenario #98) and are less likely to represent reservoir architectures; hence these scenarios can be falsified.

Fig. 26 presents examples of falsified and plausible scenarios after the scenario-based data assimilation framework. The first column shows falsified cases. Scenario #20, despite having a relatively high NTG (0.63), fails to reproduce the observed production data after ESMDA, indicating its reservoir architecture is far from the 'truth'. Scenario #21 features 500-800 m-wide channels, in contrast to the 200–500 m-wide channels in the reference scenario. The differing vertical connectivity contributes to its poor assimilation performance. The second column shows plausible scenarios, such as Scenarios #55 and #72, which exhibit similar channel dimensions and connectivity with the reference model and achieve good production data matches after ESMDA. However, plausible Scenario #18 shown in the third column exhibits high NTG values (0.69) that deviate from NTG in the reference scenario (0.51) but still produce acceptable matches with the observed well profiles. This suggests that correct results may be obtained for incorrect geological reasons. Scenario #54, which is dominated by wider channels (500-800 m), also yields reasonable fits. This is likely due to large-scale connectivity. These results highlight that while ESMDA can adjust property fields to match observed data, it may do so for geologically dissimilar scenarios. Plausible scenarios include both geologically consistent models and those with acceptable data assimilation performance for the wrong geological reasons. In contrast, falsified scenarios—identified after scenario-based data assimilation—are fundamentally inconsistent with the reference architecture. This approach effectively narrows the scenario space and reduces geological uncertainty.

4. Discussions

A geothermal reservoir entails more uncertainty due to less availability of data compared to oil and gas fields (Schulte et al., 2020). These uncertainties cannot be addressed by relying on a single geological scenario, which is likely biased (Ringrose and Bentley, 2016). In particular, there are a lot of geologically complex situations like fluvial geothermal reservoirs. This highlights the importance of scenario-based modeling, like RRM, which enables users to rapidly and efficiently generate 3D geologically consistent reservoir models from 2D sketches

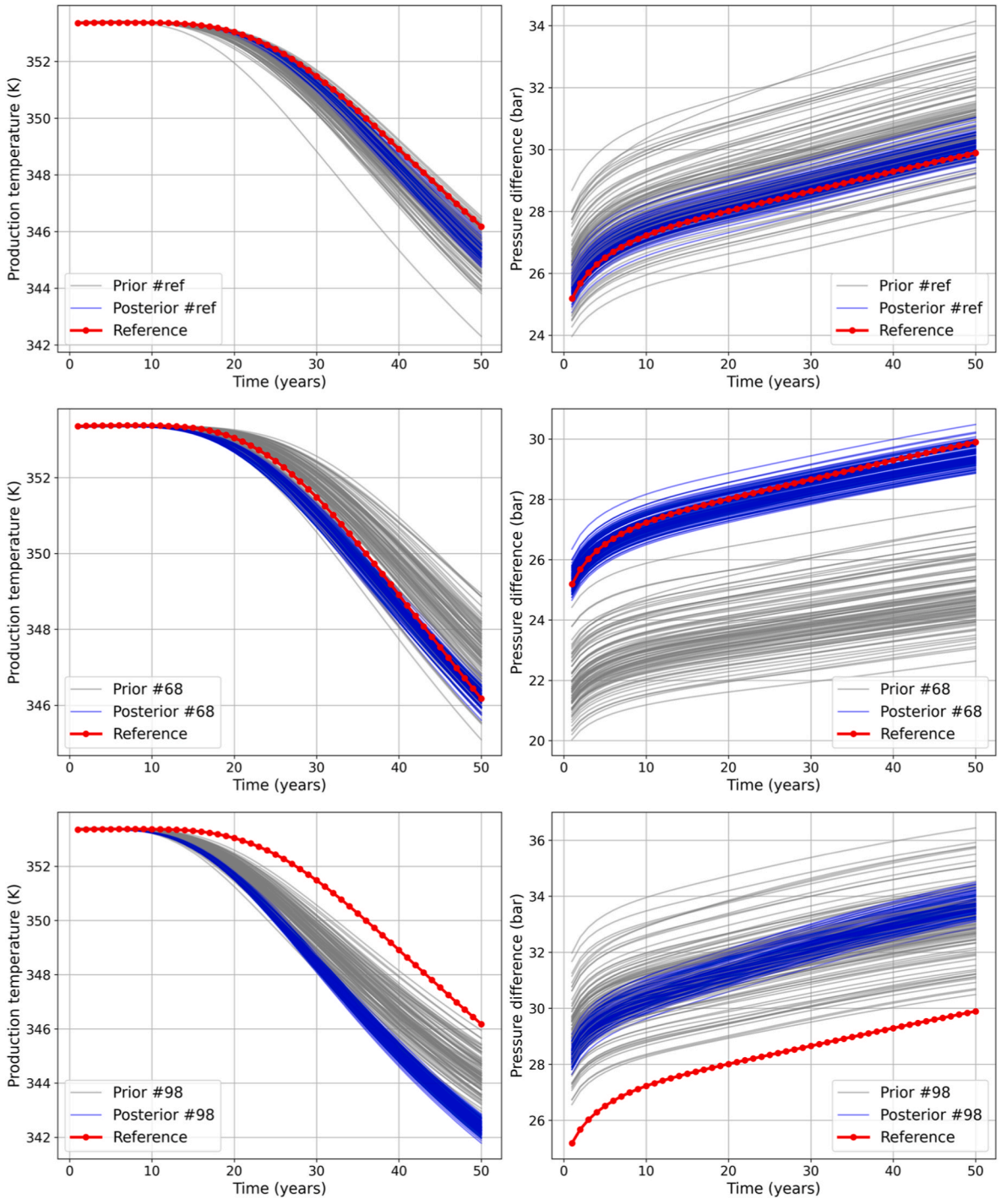

Fig. 23. Simulated production temperature and pressure differences between the injector and producer for the prior and posterior ensembles of the 'truth' scenario (1st row), Scenario #68 (2nd row), and Scenario #98 (3rd row). The red line represents the same production response from the 'truth' case. The grey lines are predictions from the prior ensemble, the blue lines are results from the posterior ensemble. (For interpretation of the references to colour in this figure legend, the reader is referred to the Web version of this article.)

(Jacquemyn et al., 2021; Petrovskyy et al., 2023). Given the complexity of fluvial reservoir systems, scenario-based RRM is innovatively utilized by creating a library of fluvial channel layer templates with varying channel features, not by directly constructing the entire reservoir model. By randomly selecting, cropping, and stacking these templates with overlapping segments that mimic sedimentary processes, a wide range of reservoir scenarios can be generated probabilistically. This approach allows for explicit control over the channel characteristics of ensemble scenarios. Furthermore, integrating scenario-based RRM with geostatistical techniques enables the joint representation of uncertainties in both reservoir architecture and petrophysical properties, forming a robust foundation for uncertainty quantification in geothermal production forecasting.

ESMDA has proven to be an effective data assimilation method, as demonstrated in Section 3.3.1, where it successfully adjusts sand facies properties to match observed data when applied to models based on the 'truth' reservoir architecture. However, its effectiveness depends heavily on how well the prior scenario represents the true reservoir

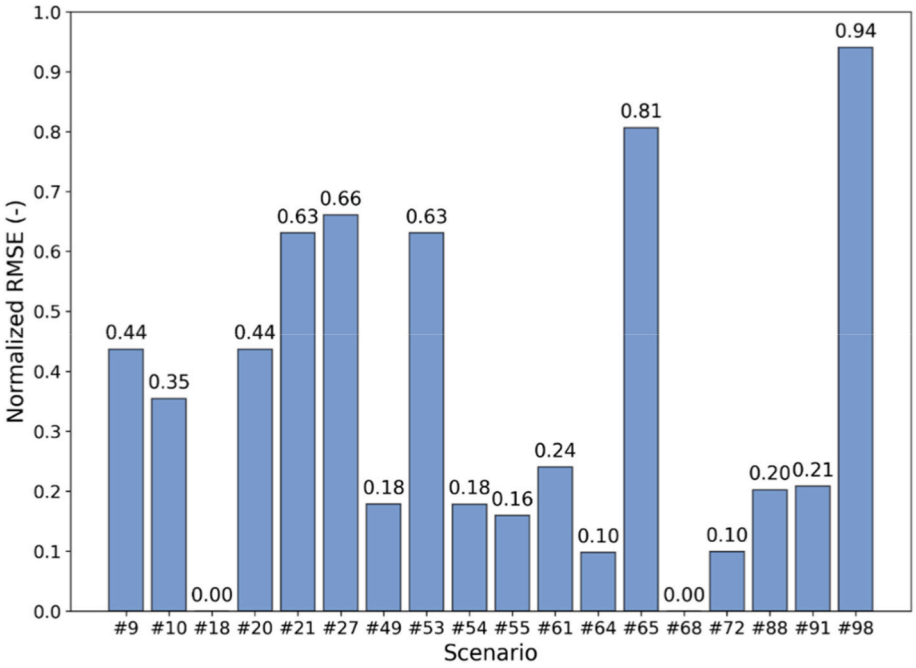

Fig. 24. Normalized *RMSE* of the simulated temperature and pressure profiles along three wells for the posterior ensembles for different scenarios, computed as a weighted combination of the normalized *RMSE*s of temperature and pressure profiles.

structure, as seen in Scenario #98, where the assimilation performance deteriorates. The high-dimensional parameter space in the subsurface leads to an ill-posed inversion problem (Wu et al., 2021). ESMDA may produce "the right results for the wrong reasons", e.g., a poor match in reservoir architecture and unrealistic property distributions that yield good alignment with observed data, as observed in Scenarios #18 and #20. The proposed scenario-based data assimilation framework turns this weakness into a strength: scenarios that fail to match observations after data assimilation are considered unlikely and therefore falsified, while plausible scenarios are retained to produce more reliable forecasts. This approach avoids over-reliance on a single, potentially biased scenario. Moreover, the posterior distribution of porosity and permeability in the sand facies can serve as an indicator of whether the reservoir architecture of a scenario is a good approximation of the geometry of the reference scenario. When the prior PDF of the properties of sand facies follows a Gaussian distribution but the posterior PDF becomes uniform (Scenario #68) or truncated (Scenario #98), it is highly likely that the reservoir architecture differs from the reservoir architecture of the reference (or 'truth') geometry. This occurs because ESMDA pushes porosity and permeability values toward their limits in the model parameterization to compensate for the mismatch in reservoir architecture while still trying to reproduce the 'observed' data. Geological scenarios with truncated posterior PDFs for porosity and permeability are hence more likely candidates to be falsified. Considering the computational demands of running ESMDA across multiple geological scenarios and ensemble realizations, high computational efficiency of the simulator is critical. For example, GPU acceleration, as has been developed for open-DARTS (Wang et al., 2023), can be used to further enhance simulation speed. The proposed scenario-based data assimilation framework is well suited for field-scale applications due to its inherent parallel structure. Each realization can be simulated independently, enabling efficient implementation on high-performance computing systems.

In fluvial reservoir systems, geological features such as channel width, channel sinuosity, and layer stacking patterns play a critical role in controlling flow and heat transport processes (Crooijmans et al., 2016). However, no consistent trends in these channel features were observed among the plausible scenarios (#18, #49, #54, #55, #61, #64, #68, #72, #88, and #91). This is likely because various combinations of layer-scale features can result in similar production responses. For example, a model with narrower but more sinuous and numerous channels may exhibit similar flow behavior to one with fewer but wider channels. Moreover, the cumulative effect of 15 stacked layers governs the overall flow and heat transfer behavior, making it difficult to isolate the impact of individual geometric features. Indicators that account for interlayer or intralayer connectivity should be employed to characterize reservoir architecture (Crooijmans et al., 2016).

There are several limitations to be addressed. Regarding the construction of geological models, only binary facies were considered, which is appropriate for a proof-of-concept study focusing on the impact of channel geometries. However, real fluvial reservoirs often contain more complex sedimentary elements, such as point bars, levees, channel lag deposits, and other internal architectural features. These facies variations introduce additional heterogeneities that can influence fluid flow and heat transport in geothermal systems (Aghaei et al., 2024). In principle, our workflow is able to account for more detailed multi-facies architectures, which would allow further investigation as to how specific sedimentary features affect geothermal production performance and data assimilation outcomes. In addition, in the current implementation, data assimilation is performed using temperature and pressure profiles recorded at three wells over time. While temperature is a useful observation, it typically responds over long timescales, and meaningful drawdown is often not observed until thermal breakthrough occurs, at which point remedial operational options are limited. Pressure, on the other hand, responds more quickly and remains relatively stable during long-term production. The pressure curves with nearly no significant changes after a few years of production provide little new insight for updating models. Moreover, the drilling of a new monitoring well is not economic. Consequently, relying solely on a few years of continuous temperature and pressure observations from a limited number of wells can lead to suboptimal data assimilation performance.

To improve early-time data availability, low-cost alternatives should be explored. One promising option is pressure response testing through shut-in and open-well cycles, which can capture dynamic pressure transients (Abdelhafiz et al., 2021). These transients offer valuable information on formation connectivity and transmissibility. Another

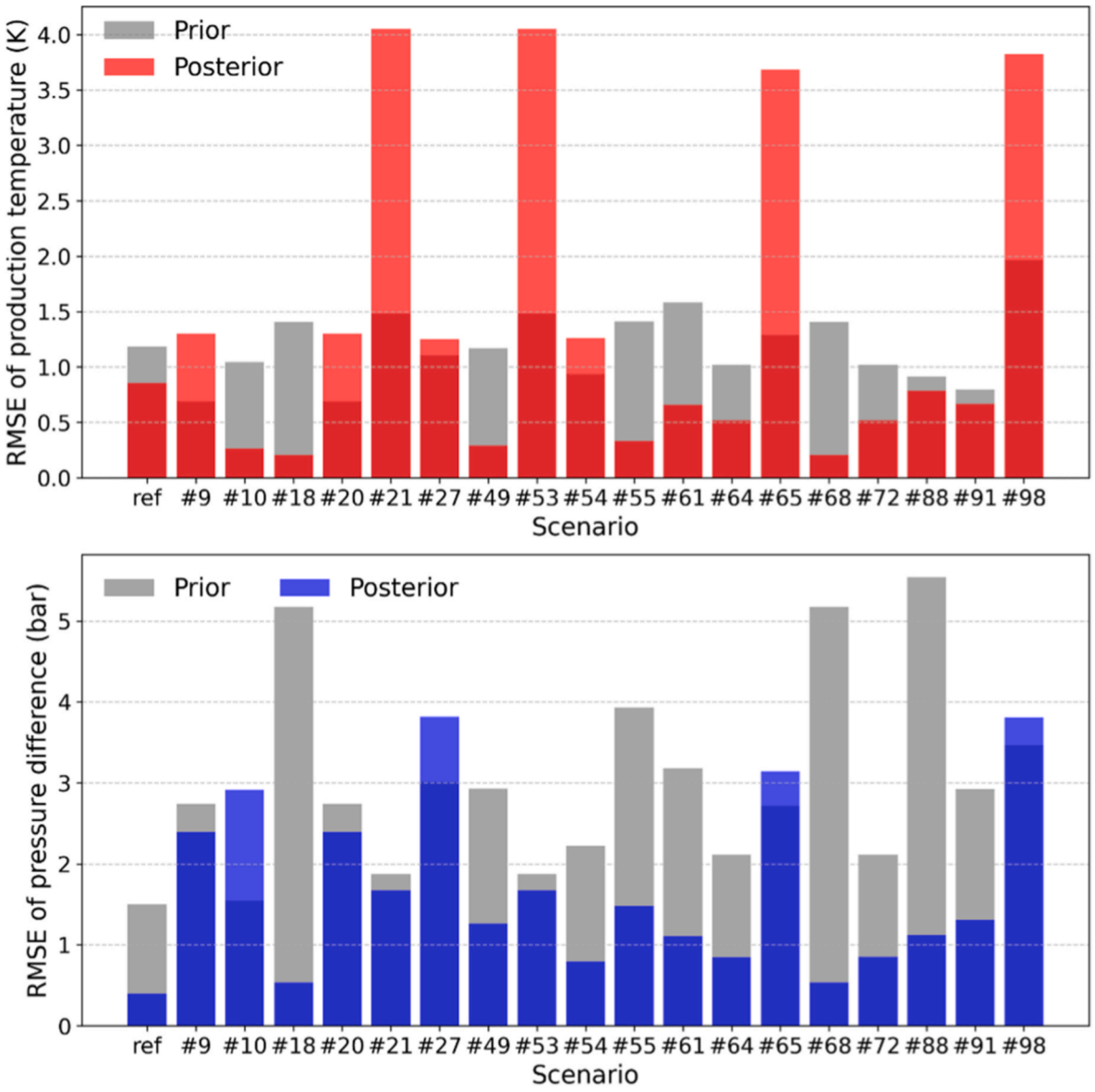

Fig. 25. *RMSE* for the production temperature (left) and pressure differences between injector and producer (right) for different scenarios after 50 years of simulated heat production.

complementary method is chemical tracer testing, which can yield concentration changes at observation wells and reveal preferential flow paths and high-permeability channel connectivity (Chen et al., 2025a; Wu et al., 2021). Simulating these physical processes is relatively straightforward to incorporate into our framework. The transport of naturally occurring or artificial tracers that are chemically inert is dominated by advective flow along connected channels and, in contrast to heat transport, does not interact with the rock itself. Hence tracer breakthrough occurs earlier and is more sensitive to the channel connectivity compared to thermal breakthrough, which allows models to be falsified earlier during the geothermal operations and enables the adjustment of operational strategies before thermal breakthrough has occurred. In addition, spatial data types such as electromagnetic or seismic surveys can provide broader coverage of the reservoir architecture (Oudshoorn et al., 2024; Schmelzbach et al., 2016). Especially seismic data is important to identify channel features and guide the construction of geological scenarios, thereby reducing geological uncertainty before production-based data assimilation begins (Gesbert et al., 2025). In the future, scenario-based data assimilation could incorporate these transient responses from cyclic shut-ins or chemical tracer simulation. The value of information is also an essential topic to identify cost-effective data acquisition strategies that offer the greatest uncertainty reduction.

5. Conclusions

In this paper, a scenario-based data assimilation framework is proposed that integrates efficient geological modeling using scenario-based Rapid Reservoir Modeling (RRM) and stochastic modeling, along with geothermal production simulation, and ESMDA. The posterior predictions improve the production estimates in complex fluvial geothermal systems. The main conclusions are drawn as follows:

1. In geological modeling of fluvial geothermal systems, uncertainties arises from both petrophysical properties and complex reservoir architecture, including channel width, sinuosity, stacking pattern, and connectivity. A limited amount of data is typically available and a full range of possible production outcomes needs to be explored. Relying solely on a single model or scenario – which is likely biased and anchored – is not sufficient to give reliable production estimates.

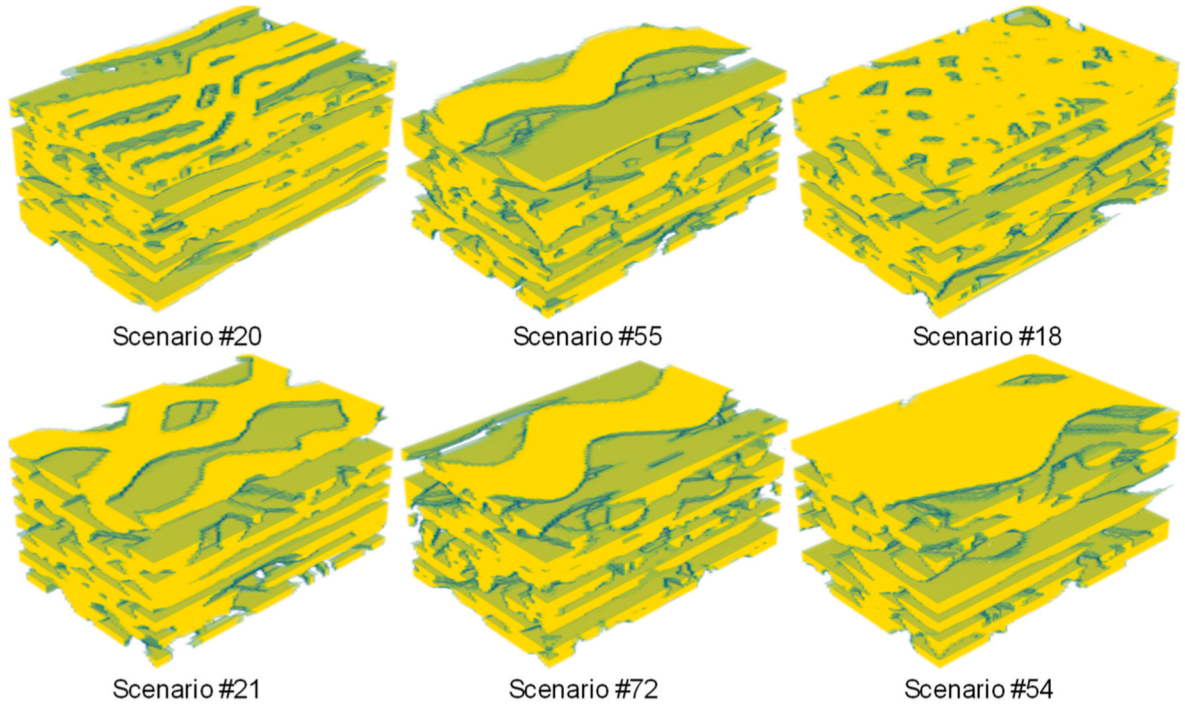

Fig. 26. 3D views of the selected reservoir scenarios. The first column shows examples of falsified scenarios (#20 and #21), which fail to reproduce the observed production data. The second and third columns show plausible scenarios (#55, #72, #18, and #54) that achieve acceptable matches after scenario-based data assimilation.

2. The combination of scenario-based RRM and stochastic modeling efficiently generates geologically-consistent fluvial scenarios and corresponding realizations that are fully constrained by well data. The RRM tool has been novelly utilized that multiple deterministic fluvial geothermal reservoir scenarios are created in a probabilistic manner by randomly selecting, cropping, and stacking channelized layers from the layer template library. Constraints such as facies logs along well paths, data from core analysis, and NTG can be incorporated into the modeling process. This approach enables rapid generation of an ensemble of deterministic geological scenarios and associated equiprobable realizations with geostatistically distributed properties, capturing uncertainty in both reservoir architecture and petrophysical characteristics. The proposed modeling method avoids limiting uncertainty analyses to a single geological scenario (i.e., base case) and therefore allows us to explore a wider range of geological uncertainties, which is key to assessing the performance of geothermal reservoirs more robustly.
3. Scenario-based ESMDA framework can be used to falsify reservoir scenarios, which helps to constrain uncertainty in production forecasts for fluvial geothermal systems. Rather than adjusting the petrophysical properties of a single reservoir scenario that could be biased, an ensemble of scenarios is simulated. Scenarios with lower data assimilation errors are retained as plausible scenarios that may represent actual reservoir architecture to predict production outcomes. However, ESMDA can yield good matches with observations for the wrong reasons – for instance, by compensating for incorrect reservoir architectures with unrealistic property adjustments. We turn this weakness into the advantages: scenarios that poorly match the observations after DA are falsified.

CRediT authorship contribution statement

Guofeng Song: Conceptualization, Formal analysis, Investigation, Methodology, Software, Validation, Visualization, Writing – original draft, Writing – review & editing. **Sebastian Geiger:** Conceptualization, Funding acquisition, Methodology, Project administration, Supervision, Writing – original draft, Writing – review & editing. **Denis Voskov:** Conceptualization, Methodology, Supervision, Writing – original draft, Writing – review & editing. **Hemmo A. Abels:** Conceptualization, Methodology, Supervision, Writing – original draft, Writing – review & editing. **Philip J. Vardon:** Conceptualization, Methodology, Supervision, Writing – review & editing.

Declaration of competing interest

The authors declare the following financial interests/personal relationships which may be considered as potential competing interests: Sebastian Geiger reports financial support was provided by Energi Simulation. If there are other authors, they declare that they have no known competing financial interests or personal relationships that could have appeared to influence the work reported in this paper.

Acknowledgments

The authors thank Guillaume Rongier for access to the Geomodpy python library for stochastic geological modeling, Yuan Chen for assistance with debugging the DARTS simulations, and Gabriel Serrao Seabra for sharing the initial ESMDA codes of the 2D reservoir example. This research was supported by the TU Delft Excellence Foundation and the Energi Simulation Chair of Sebastian Geiger. We thank the editor and reviewers for their constructive feedback and comments.

Data availability

Data will be made available on request.

References

Abdelhafiz, M.M., Hegele Jr, L.A., Oppelt, J.F., 2021. Temperature modeling for wellbore circulation and shut-in with application in vertical geothermal wells. J. Petrol. Sci. Eng. 204, 108660.

Aghaei, H., et al., 2024. Impact of Fluvial meander-belt Sedimentary Heterogeneity on the Efficiency of low-enthalpy Geothermal Doublets: Heat-Transport Simulations of Forward Stratigraphic Models. Geoenergy: geoenergy2024-024.
Anderson, A., Rezaie, B., 2019. Geothermal technology: trends and potential role in a sustainable future. Appl. Energy 248, 18–34.
Athens, N.D., Caers, J.K., 2019. A Monte Carlo-based framework for assessing the value of information and development risk in geothermal exploration. Appl. Energy 256, 113932.
Babaei, M., Nick, H.M., 2019. Performance of low-enthalpy geothermal systems: interplay of spatially correlated heterogeneity and well-doublet spacings. Appl. Energy 253, 113569.
Bai, T., Tahmasebi, P., 2022. Sequential Gaussian simulation for geosystems modeling: a machine learning approach. Geosci. Front. 13 (1), 101258.
Baird, K., et al., 2023. Assessing the impact of hierarchical geological heterogeneities on geothermal energy production. 84th EAGE Annual Conference & Exhibition. European Association of Geoscientists & Engineers, pp. 1–5.
Bentley, M., Smith, S., 2008. Scenario-based reservoir modelling: the need for more determinism and less anchoring. Future Geol. Modelling Hydrocarbon Dev. 309 (1), 145–159.
Bond, C.E., 2015. Uncertainty in structural interpretation: lessons to be learnt. J. Struct. Geol. 74, 185–200.
Cao, Z., Li, L., Chen, K., 2018. Bridging iterative ensemble smoother and multiple-point geostatistics for better flow and transport modeling. J. Hydrol. 565, 411–421.
Chen, C., et al., 2024. Deep learning-based inversion framework by assimilating hydrogeological and geophysical data for an enhanced geothermal system characterization and thermal performance prediction. Energy 302, 131713.
Chen, C., et al., 2025a. Deep learning-based inversion framework for fractured media characterization by assimilating hydraulic tomography and thermal tracer tomography data: numerical and field study. Eng. Geol. 350, 107998.
Chen, Y., Voskov, D., Daniilidis, A., 2025b. Rigorous numerical methodology and heat recovery analysis for modeling of direct use geothermal systems. Geoenergy Sci. Eng. 247, 213661.
Crooijmans, R.A., Willems, C.J., Nick, H.M., Bruhn, D., 2016. The influence of facies heterogeneity on the doublet performance in low-enthalpy geothermal sedimentary reservoirs. Geothermics 64, 209–219.
Daniilidis, A., Nick, H.M., Bruhn, D.F., 2021. Interference between geothermal doublets across a fault under subsurface uncertainty; implications for field development and regulation. Geothermics 91, 102041.
Emerick, A.A., Reynolds, A.C., 2013. Ensemble smoother with multiple data assimilation. Comput. Geosci. 55, 3–15.
Evensen, G., Vossepoel, F.C., Van Leeuwen, P.J., 2022. Data Assimilation Fundamentals: a Unified Formulation of the State and Parameter Estimation Problem. Springer Nature.
Gesbert, B., Geiger, S., Verschuur, E., Abels, H. and Song, G., 2025. Insights from Integrated Geological and Seismic Modelling of Fluvial Geothermal Reservoirs, 86th EAGE Annual Conference & Exhibition. European Association of Geoscientists & Engineers, pp. 1-5.10.3997/2214-4609.2025101348.
Guo, Q., et al., 2021. Evaluation of the benefits of improved permeability estimation on high-resolution characterization of DNAPL distribution in aquifers with low-permeability lenses. J. Hydrol. 603, 126955.
Hermans, T., Nguyen, F., Klepikova, M., Dassargues, A., Caers, J., 2018. Uncertainty quantification of medium-term heat storage from short-term geophysical experiments using Bayesian evidential learning. Water Resour. Res. 54 (4), 2931–2948.
Hoteit, H., He, X., Yan, B., Vahrenkamp, V., 2023. Uncertainty quantification and optimization method applied to time-continuous geothermal energy extraction. Geothermics 110, 102675.
Jacquemyn, C., et al., 2021. Sketch-based interface and modelling of stratigraphy and structure in three dimensions. J. Geol. Soc. 178 (4), jgs2020–j2187.
Jacquemyn, C., Jackson, M.D., Hampson, G.J., 2019. Surface-based geological reservoir modelling using grid-free NURBS curves and surfaces. Math. Geosci. 51, 1–28.
Jiang, A., Jafarpour, B., 2020. History Matching Under Uncertain Geologic Scenarios with Variational Autoencoders, ECMOR XVII. European Association of Geoscientists & Engineers, pp. 1–14.
Juliusson, E., Bjornsson, S., 2021. Optimizing production strategies for geothermal resources. Geothermics 94, 102091.
Khait, M., Voskov, D.V., 2017. Operator-based linearization for general purpose reservoir simulation. J. Petrol. Sci. Eng. 157, 990–998.
Limberger, J., et al., 2018. Geothermal energy in deep aquifers: a global assessment of the resource base for direct heat utilization. Renew. Sustain. Energy Rev. 82, 961–975.
Ling, W., Jafarpour, B., 2024. Improving the parameterization of complex subsurface flow properties with style-based generative adversarial network (StyleGAN). Water Resour. Res. 60 (11) e2024WR037630.
Liu, K., et al., 2020. A gaussian process-based iterative Ensemble Kalman Filter for parameter estimation of unsaturated flow. J. Hydrol. 589, 125210.
Lund, J.W., Toth, A.N., 2021. Direct utilization of geothermal energy 2020 worldwide review. Geothermics 90, 101915.
Mendez, M., et al., 2024. Using dynamic simulations to improve geological models: a full field integrated study of an HPHT gas field in the Norwegian Sea. SPE Norway Subsurface Conference. SPE, D011S001R005.
Moya, D., Aldás, C., Kaparaju, P., 2018. Geothermal energy: power plant technology and direct heat applications. Renew. Sustain. Energy Rev. 94, 889–901.
Nowak, M., Verly, G., 2004. The practice of sequential Gaussian simulation. Geostatistics Banff 2004. Springer, pp. 387–398.
Oudshoorn, C., Werthmüller, D., Slob, E., Voskov, D., 2024. Numerical experiment on data assimilation for geothermal doublets using production data and electromagnetic observations. Geophysics 89 (6), M227–M237.
Petrovskyy, D., et al., 2023. Rapid flow diagnostics for prototyping of reservoir concepts and models for subsurface CO2 storage. Int. J. Greenh. Gas Control 124, 103855.
Ringrose, P., Bentley, M., 2016. Reservoir Model Design, vol. 2. Springer.
Saifullin, I., Seabra, G.S., Pluymakers, A., Vossepoel, F.C., Voskov, D., 2024. Integrating geomechanical proxy models with data assimilation for energy transition applications. Geomech. Energy Environ., 100618
Schmelzbach, C., et al., 2016. Advanced seismic processing/imaging techniques and their potential for geothermal exploration. Interpretation 4 (4), SR1–SR18.
Schulte, D.O., Arnold, D., Geiger, S., Demyanov, V., Sass, I., 2020. Multi-objective optimization under uncertainty of geothermal reservoirs using experimental design-based proxy models. Geothermics 86, 101792.
Seabra, G.S., Mücke, N.T., Silva, V.L.S., Voskov, D., Vossepoel, F.C., 2024. AI enhanced data assimilation and uncertainty quantification applied to geological carbon storage. Int. J. Greenh. Gas Control 136, 104190.
Song, G., et al., 2024. Towards a subsurface geothermal digital twin: efficient construction of geological scenarios for modelling fluvial geothermal reservoirs. Fifth EAGE Global Energy Transition Conference & Exhibition (GET 2024). European Association of Geoscientists & Engineers, pp. 1–5.
Song, G., Geiger, S., Voskov, D., Abels, H.A., Vardon, P.J., 2025. Assessing the ensemble smoother with multiple data assimilation for subsurface fluvial geothermal systems. 50th Workshop on Geothermal Reservoir Engineering. Stanford University, Stanford, California.
Tas, L., et al., 2025. Efficiency and heat transport processes of low-temperature aquifer thermal energy storage systems: new insights from global sensitivity analyses. Geoth. Energy 13 (1), 2.
Tian, X., Volkov, O., Voskov, D., 2024. An advanced inverse modeling framework for efficient and flexible adjoint-based history matching of geothermal fields. Geothermics 116, 102849.
Vardon, P., et al., 2024. A research and energy production geothermal project on the TU delft campus: project implementation and initial data collection. 49th Workshop on Geothermal Reservoir Engineering. Stanford University, Stanford, California.
Verly, G., 1993. Sequential Gaussian simulation: a Monte Carlo method for generating models of porosity and permeability. Generation, Accumulation and Production of Europe's Hydrocarbons III: Special Publication of the European Association of Petroleum Geoscientists No. 3. Springer, pp. 345–356.
Voskov, D., et al., 2024. A research and production geothermal project on the TU Delft campus: initial modeling and establishment of a digital twin. 49th Workshop on Geothermal Reservoir Engineering. Stanford University, Stanford, California, Stanford University, Stanford, California.
Wang, Y., et al., 2023. Uncertainty quantification in a heterogeneous fluvial sandstone reservoir using GPU-based Monte Carlo simulation. Geothermics 114, 102773.
Wang, Y., Voskov, D., Khait, M., Bruhn, D., 2020. An efficient numerical simulator for geothermal simulation: a benchmark study. Appl. Energy 264, 114693.
Wang, Y., Voskov, D., Khait, M., Saeid, S., Bruhn, D., 2021. Influential factors on the development of a low-enthalpy geothermal reservoir: a sensitivity study of a realistic field. Renew. Energy 179, 641–651.
Willems, C.J.L., Vondrak, A., Mijnlieff, H.F., Donselaar, M.E., van Kempen, B.M.M., 2020. Geology of the Upper Jurassic to Lower Cretaceous geothermal aquifers in the West Netherlands Basin - an overview. Netherlands J. Geosci.-Geologie En Mijnbouw 99, e1.
Witter, J.B., Trainor-Guitton, W.J., Siler, D.L., 2019. Uncertainty and risk evaluation during the exploration stage of geothermal development: a review. Geothermics 78, 233–242.
Wu, H., Fu, P., Hawkins, A.J., Tang, H., Morris, J.P., 2021. Predicting thermal performance of an enhanced geothermal system from tracer tests in a data assimilation framework. Water Resour. Res. 57 (12) e2021WR030987.
Yousefzadeh, R., Kazemi, A., Ahmadi, M., Gholinezhad, J., 2020. Introduction to Geological Uncertainty Management in Reservoir Characterization and Optimization Robust Optimization and History Matching. History. Springer.